

ARTICLE

Received 23 Nov 2015 | Accepted 26 Apr 2016 | Published 27 May 2016

DOI: 10.1038/ncomms11752

OPEN

RPA and Rad51 constitute a cell intrinsic mechanism to protect the cytosol from self DNA

Christine Wolf¹, Alexander Rapp², Nicole Berndt³, Wolfgang Staroske⁴, Max Schuster¹, Manuela Dobrick-Mattheuer¹, Stefanie Kretschmer¹, Nadja König¹, Thomas Kurth^{4,5}, Dagmar Wieczorek⁶, Karin Kast⁷, M. Cristina Cardoso², Claudia Günther³ & Min Ae Lee-Kirsch¹

Immune recognition of cytosolic DNA represents a central antiviral defence mechanism. Within the host, short single-stranded DNA (ssDNA) continuously arises during the repair of DNA damage induced by endogenous and environmental genotoxic stress. Here we show that short ssDNA traverses the nuclear membrane, but is drawn into the nucleus by binding to the DNA replication and repair factors RPA and Rad51. Knockdown of RPA and Rad51 enhances cytosolic leakage of ssDNA resulting in cGAS-dependent type I IFN activation. Mutations in the exonuclease TREX1 cause type I IFN-dependent autoinflammation and autoimmunity. We demonstrate that TREX1 is anchored within the outer nuclear membrane to ensure immediate degradation of ssDNA leaking into the cytosol. In TREX1-deficient fibroblasts, accumulating ssDNA causes exhaustion of RPA and Rad51 resulting in replication stress and activation of p53 and type I IFN. Thus, the ssDNA-binding capacity of RPA and Rad51 constitutes a cell intrinsic mechanism to protect the cytosol from self DNA.

¹Department of Pediatrics, Medizinische Fakultät Carl Gustav Carus, Technische Universität Dresden, 01307 Dresden, Germany. ²Department of Biology, Technische Universität Darmstadt, 64287 Darmstadt, Germany. ³Department of Dermatology, Medizinische Fakultät Carl Gustav Carus, Technische Universität Dresden, 01307 Dresden, Germany. ⁴Biotechnology Center, Technische Universität Dresden, 01307 Dresden, Germany. ⁵Center for Regenerative Therapies, Technische Universität Dresden, 01307 Dresden, Germany. ⁶Institute of Human Genetics, Heinrich-Heine-University, Medical Faculty, 40225 Düsseldorf, Germany. ⁷Department of Gynecology, Medizinische Fakultät Carl Gustav Carus, Technische Universität Dresden, 01307 Dresden, Germany. Correspondence and requests for materials should be addressed to M.L.-K. (email: minae.lee-kirsch@uniklinikum-dresden.de)

Activation of type I interferon (IFN) initiated by innate immune sensing of nucleic acids plays a key role in the pathogenesis of autoimmunity. Cytosolic RNA and DNA are sensed by pattern-recognition receptors such as RIG-I/MDA5 and cGAS, respectively¹. As these sensors have only limited capacity to discriminate between self and non-self nucleic acids, the organism must be equipped with efficient means to avoid inappropriate immune activation through nucleic acids emanating from metabolic processes such as DNA damage repair. Reactive oxygen species and ultraviolet light continuously cause numerous DNA lesions most of which are efficiently repaired by the DNA repair machinery resulting in the excision of short single-stranded DNA (ssDNA) byproducts². However, how the cell deals with this nuclear DNA waste is largely unknown.

TREX1 is the major cytosolic exonuclease in mammalian cells and acts preferentially on ssDNA^{3,4}. Mutations in *TREX1* cause a spectrum of type I IFN-dependent autoinflammatory and autoimmune phenotypes including Aicardi-Goutières syndrome (AGS), familial chilblain lupus, retinal vasculopathy with cerebral leukodystrophy (RVCL) and systemic lupus erythematosus (SLE)^{5–9}. AGS is also caused by mutations in the ribonuclease H2 complex¹⁰, the triphosphohydrolase SAMHD1 (ref. 11) and the RNA-editing enzyme ADAR¹² highlighting the importance of the intracellular nucleic acid metabolism in the protection from autoimmunity.

Trex1^{-/-} mice develop type I IFN-mediated autoimmune disease initiated in non-hematopoietic cells and succumb to cardiac failure^{13,14}. Type I IFN activation in *TREX1*-deficient mice was shown to be caused by cGAS-dependent sensing of cytosolic DNA^{15–17}, yet the mechanisms underlying the formation of *TREX1* substrates remain controversial. In *Trex1*^{-/-} mouse embryonic fibroblasts (MEF), accrual of cytosolic ssDNA has been attributed to aberrant DNA replication intermediates induced by Ataxia telangiectasia-mutated (ATM)-dependent checkpoint activation¹⁸. Conversely, autoimmunity in *Trex*^{-/-} mice was reported to be triggered by retroelement complementary DNA (cDNA) in the absence of checkpoint signalling¹³. In fibroblasts of AGS patients with RNase H2 or SAMHD1 deficiency, defective ribonucleotide excision repair or depletion of dNTP pools, respectively, cause chronic low-level DNA damage leading to constitutive activation of p53 and type I IFN^{19,20}, raising the question as to how DNA damage signalling may be linked to type I IFN activation in *TREX1* deficiency.

Here we report that short ssDNA arising within the nucleus is retained within the nuclear compartment by binding to the ssDNA-binding proteins replication protein A (RPA) and recombination protein A (Rad51) and establish that RPA and Rad51 depletion enhances cytosolic leakage of short ssDNA leading to type I IFN activation in a cGAS-dependent manner. Furthermore, we demonstrate that *TREX1* is a tail-anchored protein inserted into the outer nuclear membrane to guard the cytosol from nuclear self DNA. In *TREX1*-deficient patient cells, accrual of ssDNA causes exhaustion of RPA and Rad51 resulting in replication stress and DNA damage checkpoint signalling alongside type I IFN activation. Thus, these findings delineate a novel mechanism that links pathways of DNA replication and repair with innate immune activation in the pathogenesis of autoimmunity.

Results

RPA and Rad51 prevent cytosolic leakage of short ssDNA.

To investigate the transit of short ssDNA across the nuclear membrane, we microinjected a 30-bp ATTO647N-labelled DNA oligonucleotide (ssDNA647N) into the cytoplasm or the nucleus of HEK293T cells. Microinjection into the cytoplasm resulted in

rapid nuclear accumulation of the ssDNA647N oligonucleotide (Fig. 1a). In contrast, if ssDNA647N was microinjected into the nucleus, the fluorescent signal remained nuclear (Fig. 1b). Intriguingly, in cells with two nuclei, one of which was microinjected with ssDNA647N, the non-injected nucleus became fluorescent over time indicating leakage of the oligonucleotide into the cytosol and subsequent uptake by the non-injected nucleus (Fig. 1c and Supplementary Movie 1). We, therefore, hypothesized that short ssDNA, albeit capable of passively or actively crossing the nuclear membrane, is retained within the nucleus by binding to nuclear proteins.

DNA processing during replication and repair requires the ssDNA-binding proteins RPA and Rad51 to protect ssDNA stretches from nucleolytic degradation, to prevent reannealing and to coordinate assembly of processing factors. The RPA heterotrimer binds ssDNA with an occluded length of 30 nucleotides²¹, while Rad51 recombinase forms nucleofilaments on ssDNA binding²². We, therefore, examined whether knockdown of RPA and Rad51 would alter the subcellular distribution of the ssDNA647N oligonucleotide. Following microinjection of ssDNA647N into the nucleus of HeLa cells with small interfering RNA (siRNA)-induced knockdown of RPA and Rad51, the fluorescent signal spread throughout the cytosol, while it remained confined to the nucleus in cells treated with negative control siRNA (Fig. 1d) indicating that a reduction of the nuclear pools of RPA and Rad51 causes enhanced leakage of ssDNA into the cytosol.

Depletion of RPA and Rad51 activates type I IFN. The nucleotidyl transferase cGAS is a potent sensor of cytosolic double-stranded DNA (dsDNA), but can also be activated by short ssDNA^{23–25}. Given our observation that depletion of RPA and Rad51 results in enhanced cytosolic leakage of short ssDNA, we examined whether knockdown of RPA and Rad51 is sufficient to cause type I IFN activation. siRNA-induced depletion of RPA and Rad51 in HeLa cells led to IRF3 phosphorylation and type I IFN activation as shown by increased IFN- β production and up-regulation of IFN-stimulated genes (ISG) (Fig. 1e,f and Supplementary Fig. 1a). Type I IFN activation was markedly suppressed in cells with additional knockdown of cGAS indicating that ssDNA oozing out from the nucleus engages the cytosolic DNA sensor cGAS (Fig. 1e,f). Furthermore, analysis of transcriptome data retrieved from the GEO database revealed ISG upregulation in MEFs with short hairpin RNA-induced knockdown of RPA (accession number GSE38412) (ref. 26) and in human MCF-10A cells with short hairpin RNA-induced knockdown of Rad51 (accession number GSE54266) (ref. 27), respectively, consistent with a transcriptional signature due to spontaneous IFN production (Supplementary Fig. 1b,c).

Heterozygous loss-of-function mutations in the Rad51 paralogue *RAD51C* are a rare cause of breast and ovarian cancer²⁸. Since Rad51 depletion enhances type I IFN signalling *in vitro*, we examined patients with breast or ovarian cancer due to *RAD51C* mutation for signs of autoimmunity. Intriguingly, three out of four patients were found to present with autoimmune features such as antinuclear antibodies, autoimmune thyroid disease or an IFN signature in blood (Supplementary Table 1). Taken together, these findings indicate that depletion of RPA and Rad51 promotes cytosolic accrual of ssDNA which triggers type I IFN signalling.

Accumulation of ssDNA exhausts RPA and Rad51.

In *TREX1* deficiency, type I IFN activation and autoimmunity result from immune recognition of unmetabolized cytosolic ssDNA. In line with previous findings in *Trex1*^{-/-} MEFs¹⁸, immunostaining of ssDNA in *TREX1*-deficient patient fibroblasts revealed a marked

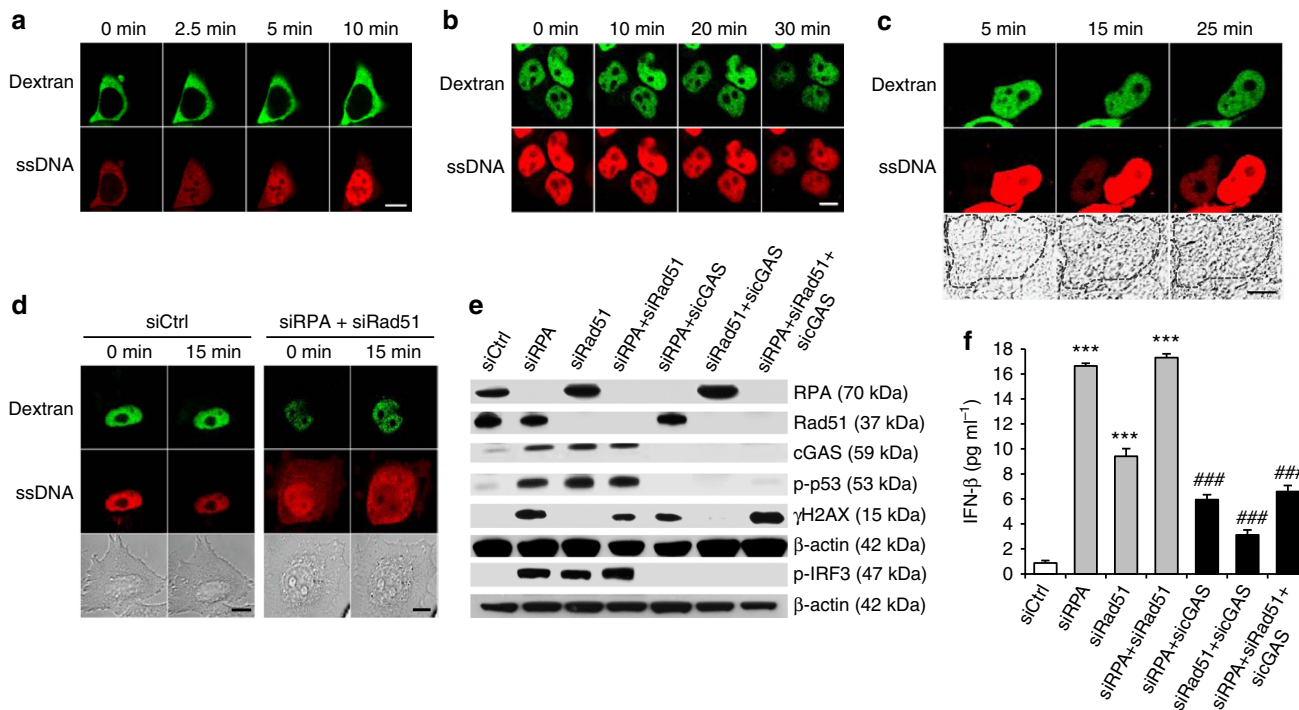


Figure 1 | The ssDNA-binding of RPA and Rad51 prevents type I IFN activation caused by leakage of nuclear ssDNA into the cytosol. (a,b) The cytoplasm (a) or the nucleus (b) of HEK293T cells was microinjected with ssDNA647N (ssDNA, red) and FITC-dextran (dextran, green) as tracer. Images were taken at the indicated time points. Scale bar, 10 μ m. (c) Representative image of a binuclear HEK cell. Fluorescence of ssDNA647N (ssDNA, red) microinjected into one nucleus, marked by FITC-dextran (dextran, green), is taken up by the non-injected adjacent nucleus. Scale bar, 10 μ m. (d) ssDNA647N (ssDNA) microinjected into nuclei of HeLa cells with knockdown of RPA70 and Rad51 (siRPA + siRad51) leaks into the cytosol within 15 min, but remains nuclear in cells transfected with negative control siRNA (siCtrl). Co-injected FITC-dextran (green) marks the injected compartment. Scale bar, 10 μ m. (e,f) Phosphorylation of IRF3 and p53 (e) as well as IFN- β induction (f) after knockdown of RPA70 and Rad51 (siRPA, siRad51) is suppressed by additional knockdown of cGAS. siCtrl, negative control siRNA. (f) Shown are the means of one experiment run in triplicates out of two independent experiments. Error bars, s.d. *** $P < 0.001$ versus siCtrl. #### $P < 0.001$ versus knockdown of RPA70, Rad51 or RPA70 and Rad51, respectively, by analysis of variance followed by Tukey' *post hoc* test.

signal both within the cytosol and the nucleus, while ssDNA was barely detectable in wild-type cells. ssDNA was undetectable in TREX1-deficient cells pretreated with S1 nuclease confirming specific staining of ssDNA (Fig. 2a). To further define the size range of the accumulating ssDNA in patient cells, we employed the halo assay, which is based on the size-dependent diffusion of DNA fragments out of agarose-embedded nuclei²⁹. Transfection of fibroblasts with increasing amounts of a 45-bp oligonucleotide resulted in increasing halo diameters in a dose-dependent manner (Supplementary Fig. 2). We next assessed halo formation in TREX1-deficient fibroblasts and observed larger halo diameters compared with wild-type cells indicating enhanced levels of short DNA molecules within the nucleus (Fig. 2b).

To explore whether ssDNA accumulating in TREX1-deficient fibroblasts is bound by RPA and Rad51, we performed automated high-content imaging. Unlike wild-type cells, patient fibroblasts exhibited an increased number of nuclear RPA foci, which decreased on extraction of cells with detergent (Fig. 2c), indicating the presence of an ssDNA-bound RPA fraction not associated with chromosomal DNA. To validate this further, we measured the mobility of RPA complexes in living cells transfected with GFP-RPA32 using raster image correlation spectroscopy (Supplementary Fig. 3). In non S-phase cells, the mean diffusion coefficient of GFP-RPA32 was significantly lower in AGS cells ($8.2 \pm 1.7 \mu\text{m}^2 \text{s}^{-1}$) than in wild-type cells ($11.9 \pm 2.8 \mu\text{m}^2 \text{s}^{-1}$) indicating that RPA is part of a larger complex in AGS cells. In S-phase cells, RPA is present in two

forms, free RPA and focal RPA engaged in replication. Again the AGS cells exhibited a reduced RPA diffusion compared to wild type cells (2.2 ± 0.9 versus $3.6 \pm 1.0 \mu\text{m}^2 \text{s}^{-1}$), while the RPA fraction engaged in replication foci exhibited nearly no mobility in both patient and wild-type cells (0.3 ± 0.6 versus $0.3 \pm 0.3 \mu\text{m}^2 \text{s}^{-1}$). In addition, we quantified the amount of ssDNA, RPA and Rad51 using high-resolution imaging following immunofluorescence (Supplementary Fig. 4). This confirmed markedly enhanced levels of ssDNA in the cytoplasm of AGS cells compared with wild-type controls. Moreover, we observed an increased co-localization between ssDNA and RPA or Rad51, respectively, in the cytoplasm of TREX1-deficient patient fibroblasts, while there was no difference in co-localization within the nucleus. Finally, we determined the intensity ratio between ssDNA and RPA or Rad51, respectively, and found an approximately twofold increase in AGS cells compared with wild-type cells suggesting an exhaustion of cellular RPA and RAD51 pools (Supplementary Fig. 4).

Furthermore, TREX1-deficient fibroblasts also showed an increased nuclear Rad51 intensity compared with wild-type cells consistent with enhanced formation of Rad51 complexes (Fig. 2d). Although TREX1-deficient cells did not harbour more Rad51 foci than wild-type cells, foci were more evenly distributed throughout the cell cycle as shown by DNA content analysis (Fig. 2e and Supplementary Fig. 5) indicating Rad51 nucleofilament formation independent of homologous recombination repair in G₂. Thus, increased formation of ssDNA

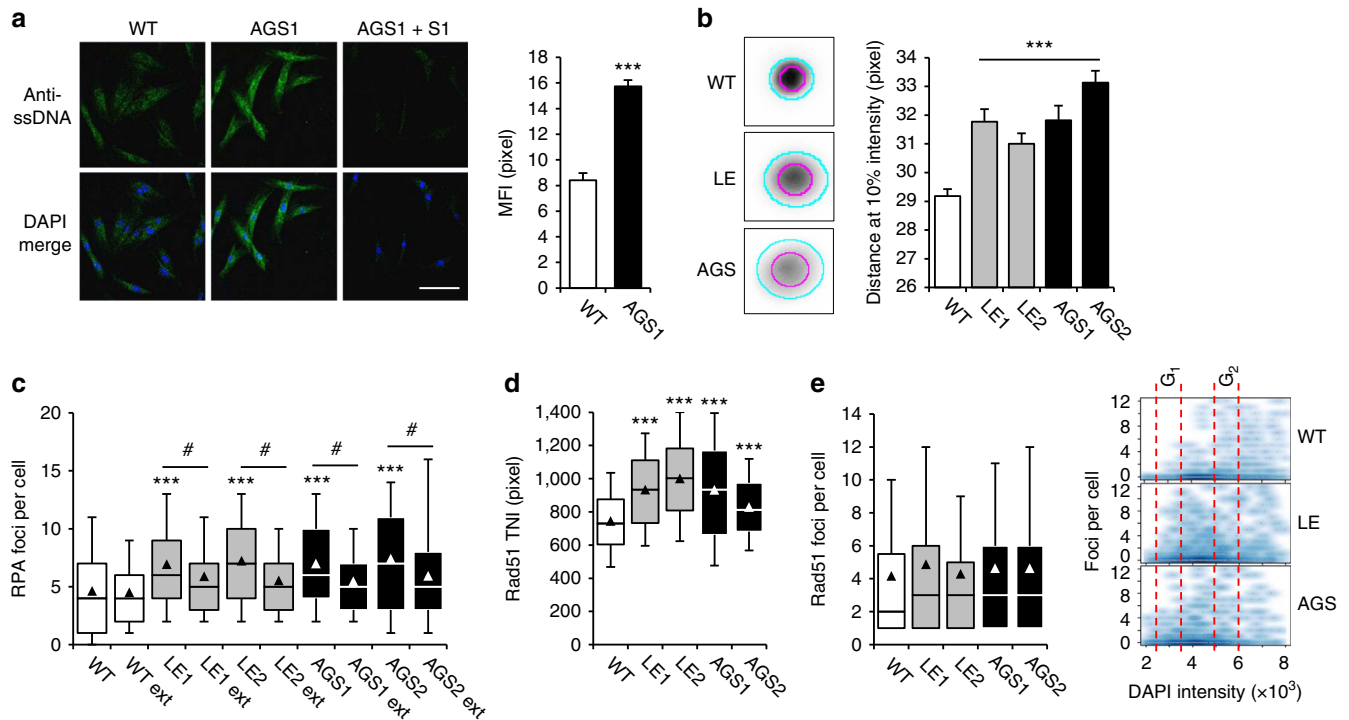


Figure 2 | TREX1-deficient cells accumulate short ssDNA in the cytosol and nucleus and exhibit enhanced ssDNA-binding of RPA and Rad51. (a) Accumulation of ssDNA in the cytoplasm and nucleus of patient (AGS1) compared with wild-type (WT) cells visualized by immunostaining (anti-ssDNA, green, left). AGS1 cells pretreated with S1 nuclease (AGS1 + S1) were stained as control. Nuclei are counterstained with DAPI (blue). Scale bar, 100 μ m. Mean fluorescence intensities (MFI) are depicted on the right. Data are from at least three independent experiments. Error bars, s.e.m. *** P < 0.001. (b) Perinuclear halo formation in TREX1-deficient (LE, AGS) and WT fibroblast nuclei. Indicated are the diameters of at 50% (magenta) and 10% (cyan) of the maximum intensities (left). Quantification of halo size at 10% maximum intensity (right). Shown are the means of two independent experiments for each patient (LE1, LE2, AGS1 and AGS2) and WT controls ($n = 2$). Error bars, s.e.m. *** P < 0.001. (c) Nuclear RPA foci formation without and after detergent extraction (ext). *** P < 0.05 versus WT; # P < 0.001 versus non-extracted nuclei. (d) Total nuclear intensity (TNI) of Rad51. (e) Nuclear Rad51 foci in TREX1-deficient cells distribute more evenly throughout the cell cycle as shown by DNA (DAPI) content analysis. (c–e) WT controls ($n = 2$). Box plots indicate the interquartile range (25–75%) from at least two independent experiments. Solid lines, median. Triangles, mean. Whiskers, 10–90th percentiles. * P < 0.05; *** P < 0.001 versus WT, Kruskal-Wallis test.

in TREX1-deficient patient cells leads to enhanced occupation of RPA and Rad51 by ssDNA exhausting the nuclear pool of RPA and Rad51.

TREX1 is a tail-anchored protein. TREX1 associates with the endoplasmic reticulum (ER) that requires the C terminus containing a predicted transmembrane helix. ER localization is functionally indispensable as truncating TREX1 mutations that preserve nuclease activity, but abrogate ER targeting cause RVCL and SLE^{7,8}. Although the C terminus of TREX1 is sufficient to confer ER localization, it was suggested that TREX1 is not a transmembrane protein¹³. We, therefore, investigated the membrane topology of TREX1 by fluorescence protease protection assay³⁰. Treatment of permeabilized HeLa cells co-expressing GFP-TREX1 and TREX1-mCherry with proteinase K led to rapid loss of green fluorescent protein (GFP) fluorescence, while the C-terminal mCherry-tag was protected from proteolysis (Fig. 3a,b) indicating membrane integration of TREX1. We excluded different bleaching properties of GFP and mCherry by showing similar fluorescence decay curves (Supplementary Fig. 6). To further confirm transmembrane orientation of TREX1, we determined that glycosylation of *in vitro* translated wild-type TREX1 (FLAG-TREX1-wt-glyc) and the truncation mutant D272fs (FLAG-TREX1-D272fs-glyc), respectively, fused to a bovine opsin fragment containing two glycosylation sites at the C-terminal end (Fig. 3c,d). Consistent with orientation of the

C terminus into the ER lumen, FLAG-TREX1-wt-glyc was glycosylated in the presence of microsomal membranes as shown by the appearance of two additional bands of higher molecular weight that disappeared after treatment with endoglycosidase H (Fig. 3d). In contrast, FLAG-TREX1-D272fs-glyc, which lacks the transmembrane helix and is not targeted to the ER^{7,8}, was not glycosylated (Fig. 3d). Electron microscopy of immunogold-labelled GFP-TREX1 in HeLa cells revealed TREX1 localization along the outer nuclear membrane and the cytosolic site of the ER membrane (Fig. 3e) as well as formation of organized smooth ER, highly organized structures typically induced by overexpression of ER membrane proteins (Fig. 3f,g)³¹. Thus, TREX1 is a tail-anchored protein with the nuclease domain facing the cytosol.

Reduced cytosolic exonuclease activity in patient cells. To gain further insight into the *in situ* biochemistry of TREX1, we first examined the interaction of YFP-TREX1 with endogenous cytosolic DNA stained with the fluorescent nucleic acid stain Sytox Orange by fluorescence lifetime imaging microscopy. The lifetime of YFP-TREX1, but not YFP alone, significantly decreased in the presence of Sytox Orange (Fig. 4a). Preincubation of cells with DNase I before Sytox Orange staining abolished the lifetime reduction of YFP-TREX1 confirming that TREX1 interacts with endogenous cytosolic DNA *in situ* (Fig. 4a). We next analysed the 3'-exonuclease activity in living

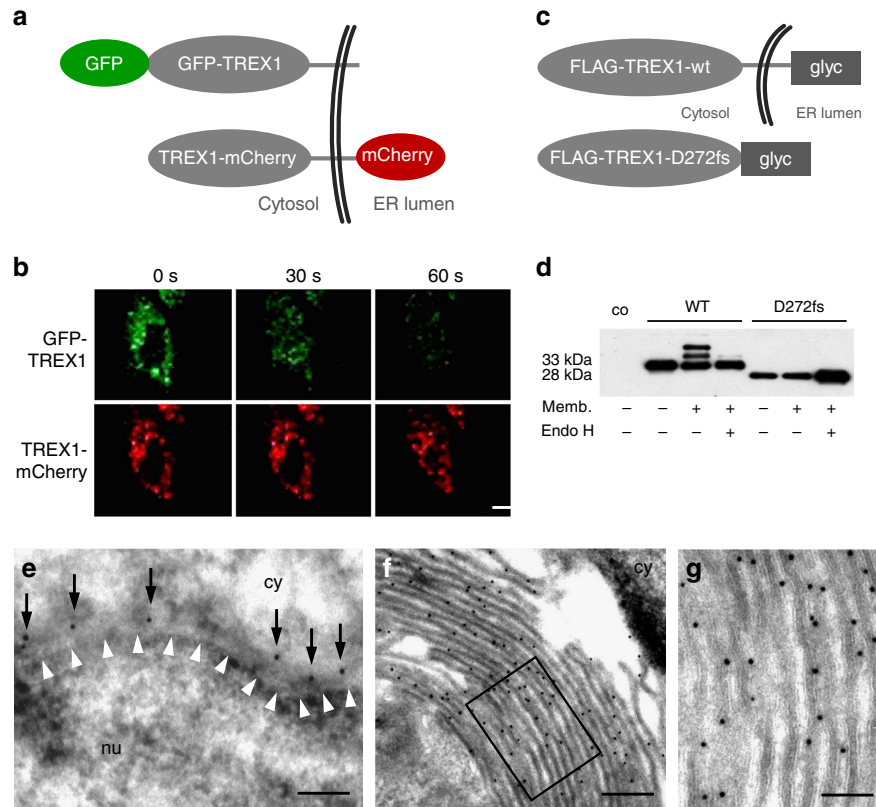


Figure 3 | TREX1 is a tail-anchored protein. (a) Schematic of fluorescently tagged TREX1 constructs used for fluorescence protease protection assay. (b) Confocal images of living HeLa cells co-expressing GFP-TREX1 and mCherry-TREX1. Proteinase K treatment after selective plasma membrane permeabilization leads to rapid dissipation of cytosolic GFP fluorescence, while mCherry resists proteolysis. Scale bar, 20 μ m. (c) Schematic of TREX1 constructs containing a C-terminal bovine opsin fragment with two N-linked glycosylation sites (glyc) used for glycosylation reporter assay. (d) *In vitro* translated WT FLAG-TREX1-wt-glyc, but not mutant FLAG-TREX1-D272fs-glyc lacking the transmembrane domain, is glycosylated in the presence of microsomal membranes (memb.) as visualized by anti-FLAG immunoblotting. Glycosylation of WT TREX1 is removed by endoglycosidase H (endo H). (e) Electron microscopy of immunogold-labelled GFP-TREX1 in HeLa cells shows expression of TREX1 (black dots marked by arrows) along the outer nuclear membrane and the cytosolic site of the ER membrane. White arrowheads indicate the inner nuclear membrane. Scale bar, 200 nm. (f) Formation of organized smooth ER consisting of lamellar stacks, branching tubules or whorls in cells overexpressing GFP-TREX1. Scale bar, 200 nm. (g) Magnification of the inset in (f) shows an even distribution of GFP-TREX1 at the extraluminal site of the ER. Scale bar, 100 nm. co, no lysate control; cy, cytoplasm; nu, nucleus.

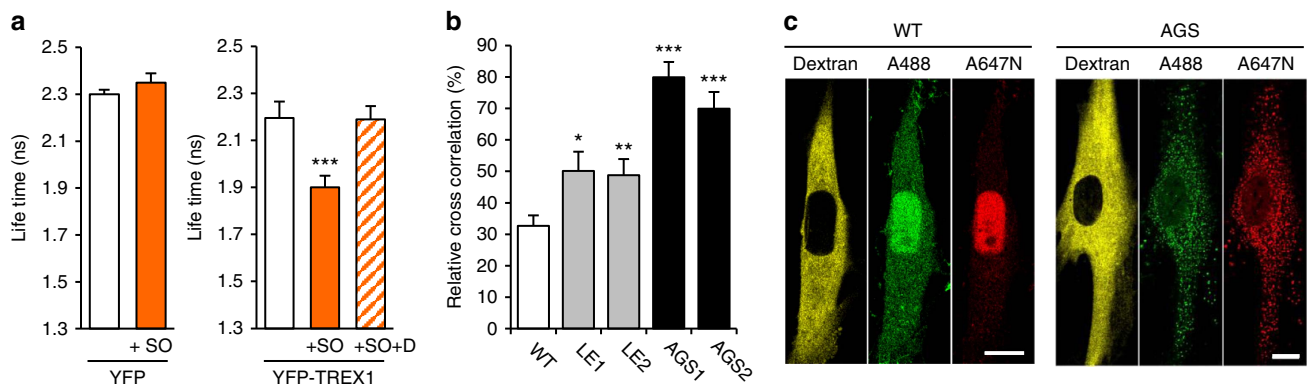


Figure 4 | *In situ* biochemistry of TREX1-deficient cells. (a) Interaction of YFP-TREX1 with endogenous cytosolic nucleic acids in HeLa cells analysed by FLIM-FRET. The fluorescence lifetime of YFP-TREX1 (right), but not of YFP alone (left), decreases significantly in the presence of Sytox Orange (+ SO). The lifetime reduction of YFP-TREX1 is abolished in cells pretreated with DNase I (+ SO + D). At least ten cells were measured per experiment. Means and s.d. of three independent experiments. *** $P < 0.001$. (b) FCCS of HeLa cells microinjected with dsDNA488_647N. Mean cross-correlation and s.e.m. of three independent experiments measured at $t < 60$ min. (WT, $n = 2$). * $P < 0.05$; ** $P < 0.01$; *** $P < 0.001$. (c) Representative FCCS images. ATTO488 (A488, green), ATTO647N (A647N, red). Rhodamine B-dextran (yellow) marks the microinjected cytosol. Scale bar, 10 μ m.

cells by fluorescent cross-correlation spectroscopy using a dual-labelled 30 bp dsDNA oligonucleotide with 3'-overhangs (dsDNA488_647N) as substrate. In wild-type fibroblasts,

microinjection of dsDNA488_647N into the cytoplasm led to a decline of cross-correlation amplitudes by 70% within few minutes and to spreading of the green and red fluorescence

throughout the cell indicating rapid nucleolytic degradation (Fig. 4b,c). In contrast, cross-correlation decayed significantly slower in fibroblasts from an AGS patient consistent with decreased cytosolic exonuclease activity (Fig. 4b). Moreover, the nucleus did not become fluorescent over the course of 60 min (Fig. 4c) suggesting that the undegraded dsDNA oligonucleotide was not capable of crossing the nuclear membrane or that the nuclear ssDNA-binding capacity was already exhausted in AGS patient cells.

DNA damage signalling and type I IFN activation in patient cells.

RPA-coated ssDNA at sites of DNA damage initiates checkpoint signalling³², while global exhaustion of nuclear RPA pools causes replication fork stalling that promotes DNA damage³³. Rad51 plays an important role in DNA damage tolerance as it participates in replicative repair of single-strand DNA lesions and replication fork reversal^{34,35}. Given enhanced ssDNA binding of RPA and Rad51 in patient cells, we hypothesized that depletion of unbound RPA and Rad51 could cause secondary DNA damage. We, therefore, investigated the overall genome integrity of fibroblast from AGS and SLE patients by alkaline single-cell gel electrophoresis, which detects alkali-labile sites such as single-strand DNA breaks, abasic sites or incomplete

excision repair sites, as well as stalled replication forks. In the absence of exogenous genotoxic stress, patient fibroblasts harboured significantly more DNA damage compared with wild-type cells as shown by the formation of longer comets (Fig. 5a). Co-staining of phosphorylated histone H2AX (γ H2AX) and p53-binding protein 1 (53BP1) did not reveal an increase in DNA double-strand breaks in TREX1-deficient cells (Supplementary Fig. 7e). However, the number of cells with diffuse pan-nuclear γ H2AX staining was markedly enhanced consistent with single-strand DNA damage (Fig. 5b and Supplementary Fig. 7f).

To further investigate the consequences of chronic DNA damage in TREX1-deficient fibroblasts, we examined their cellular phenotype. Patient cells proliferated slower than wild-type cells due to defective G₁/S transition (Fig. 5c and Supplementary Fig. 7a,b). This was accompanied by induction of the tumour suppressors p53, p16 and p21 as well as the DNA damage signalling kinases ATM and Chk1 (Fig. 5d, and Supplementary Fig. 7c,d). In addition, patient cells displayed a marked increase of senescence-associated β -galactosidase-positive cells with an enlarged morphology (Fig. 5e). Simultaneously, patient fibroblasts exhibited constitutive IRF3 phosphorylation and transactivation of an IFN- β reporter (Fig. 5d,f). Transcriptional profiling confirmed upregulation of both

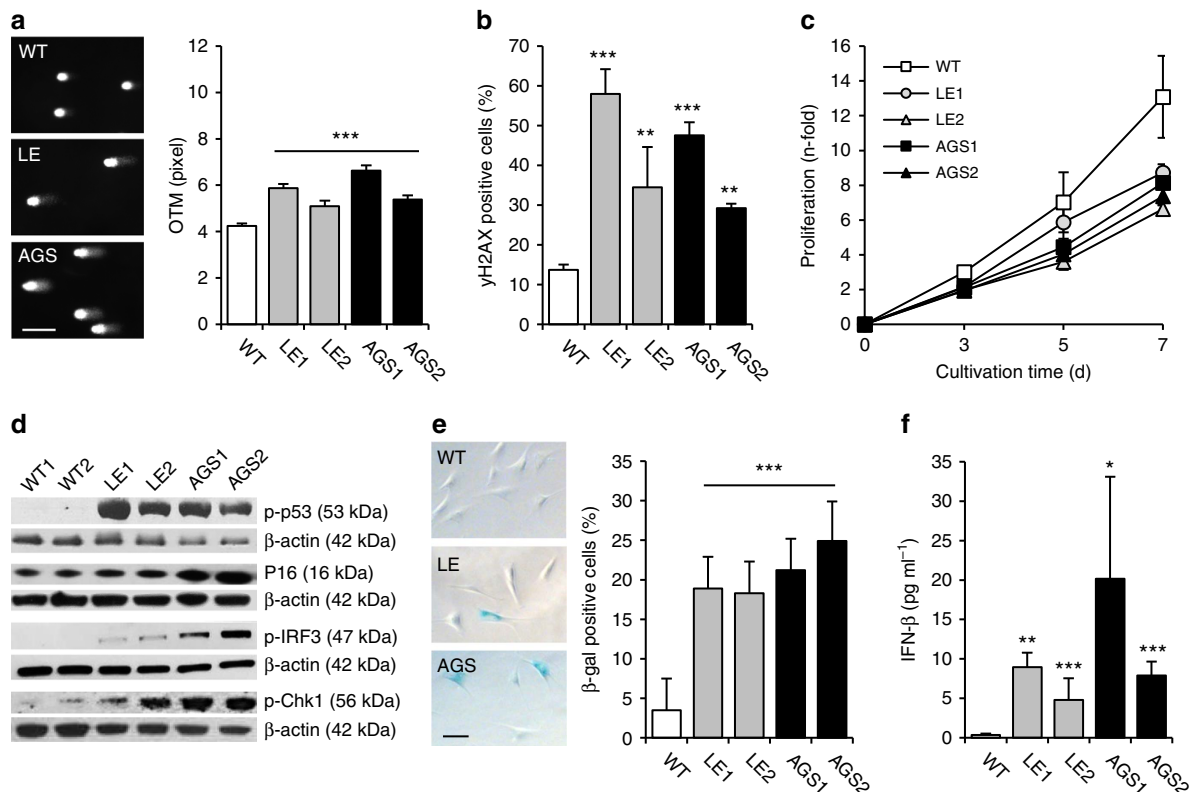


Figure 5 | Constitutive DNA damage and type I interferon activation in TREX1-deficient cells. (a) Alkaline single-cell electrophoresis depicting DNA damage in patient fibroblasts (LE, AGS) as shown by formation of longer comets with deformed nuclei compared with wild type cells (WT). Scale bar, 100 μ m (left). The Olive tail moment (OTM) corresponds to the amount of DNA fragmentation (right). Means and s.e.m. of two independent experiments for each patient (LE1, LE2, AGS1, AGS2) and WT control cell lines (WT, $n = 2$). *** $P < 0.001$. (b) Increased pan-nuclear γ H2AX-staining in TREX1-deficient fibroblasts determined by flow cytometry. Means and s.d. of at least three independent experiments for each patient (LE1, LE2, AGS1, AGS2) and WT controls (WT, $n = 5$). ** $P < 0.01$; *** $P < 0.001$. (c) Growth curves of TREX1-deficient fibroblasts (LE1, LE2, AGS1, AGS2) and WT cells ($n = 5$). * $P < 0.05$ (LE1) and ** $P < 0.01$ (LE2, AGS1, AGS2) versus WT at day 7. (d) Immunoblot analysis of unstressed patient fibroblasts (LE1, LE2, AGS1, AGS2) showing activation of p53 (p-p53; Ser15), p16, Chk1 (p-Chk1; Ser345) as well as IRF3 (p-IRF3). β -actin was probed as a loading control. (e) Senescent phenotype of patient fibroblasts (LE1, LE2, AGS1, AGS2) as shown by an increased percentage of β -galactosidase-positive cells (WT, $n = 4$; left) and representative images of senescent cells (right). Scale bar, 100 μ m. Means and s.d. of at least three independent experiments. * $P < 0.05$; ** $P < 0.01$; *** $P < 0.001$. (f) IFN- β secretion over 24 h. (WT, $n = 4$). Means and s.e.m. of five independent experiments. * $P < 0.05$; ** $P < 0.01$; *** $P < 0.001$ versus WT.

p53-dependent and ISG (Supplementary Fig. 8). Notably, siRNA-induced knockdown of TREX1 in HeLa cells was sufficient to induce both activation of p53 and type I IFN, which was abrogated in cells with additional knockdown of STING, a key signalling molecule of the cytosolic DNA sensing pathway (Fig. 6a,b). In contrast, constitutive activation of type I IFN and DNA damage signalling could be rescued in fibroblasts of an AGS patient by overexpression of wild type TREX1 (Supplementary Fig. 9). Moreover, in TREX1-deficient patient fibroblasts, knockdown of RPA and Rad51 led to a further increase in type I IFN production that was markedly suppressed by additional knockdown of cGAS (Fig. 6c), suggesting that RPA, Rad51 and TREX1 function along the same pathway to prevent accumulation of nuclear DNA within the cytosolic compartment. Binding of unmetabolized ssDNA by RPA and Rad51 causes chronic consumption of RPA and Rad51, which results in genomic instability. Collectively, these findings delineate a cell-autonomous link between a p53-dependent DNA damage response and cGAS-STING-IRF3-dependent innate immune activation in TREX1 deficiency.

TREX1-deficient cells are DNA repair-proficient. The DNA damage phenotype of TREX1-deficient cells and the finding that the AGS-causing genes, *RNASEH2* and *SAMHD1*, function in

pathways of DNA replication and repair^{19,20,36,37}, suggested that TREX1 notwithstanding its cytosolic localization might be involved in DNA replication or repair. We, therefore, investigated the role of TREX1 in processes of DNA replication and repair in more detail. First, we examined distribution of GFP-tagged TREX1 throughout the cell cycle in HeLa cells stably expressing mCherry-tagged proliferating-cell nuclear antigen, a central component of the replication machinery. While GFP-RNASEH2B, a subunit of the genome surveillance enzyme RNase H2, was recruited to replication foci during S-phase, GFP-TREX1 did not associate with replication sites (Supplementary Fig. 10a,b). Furthermore, TREX1 was not recruited to sites of hydroxyurea-induced DNA damage as shown by co-staining of γ H2AX and 53BP1 (Supplementary Fig. 10c). Second, we examined the effects of genotoxic stress in patient fibroblasts. We measured formation of cyclobutane pyrimidine dimers (CPDs), the most abundant primary photolesions, and of secondary DNA double-strand breaks in response to solar-simulated ultraviolet radiation. Irradiation with ultraviolet light led to a slightly increased formation of CPDs and DNA double-strand breaks in patient fibroblasts compared with wild-type cells (Fig. 6d), suggesting that pre-existing genomic instability or the exhaustion of essential DNA repair factors renders TREX1-deficient cells more vulnerable to exogenous genotoxic stress. However, both lesions were equally efficiently

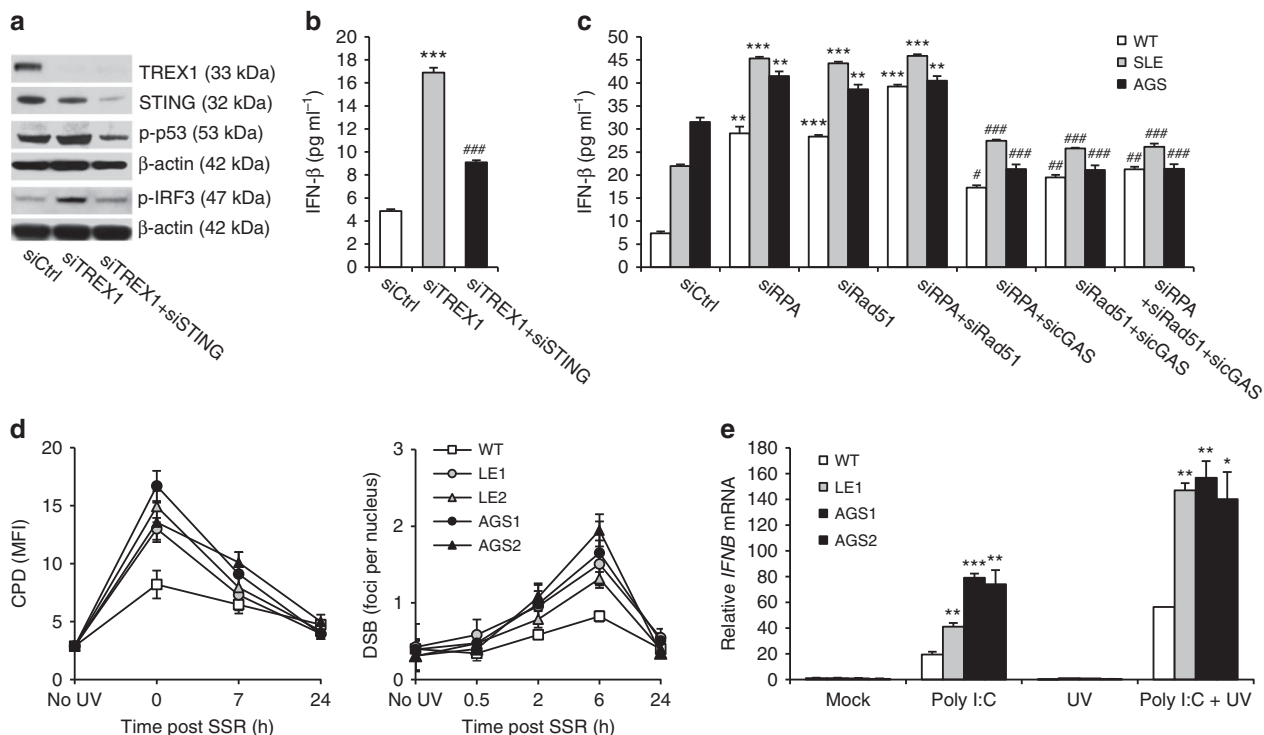


Figure 6 | TREX1-deficient cells are DNA repair-proficient, but more sensitive to type I interferon-dependent stimuli. (a,b) Knockdown of TREX1 (siTREX1) in HeLa cells causes phosphorylation of p53 and IRF3 along with induction of IFN- β . This is abrogated in cells with additional knockdown of STING (siTREX1 + siSTING). siCtrl, negative control siRNA. *** $P < 0.001$ versus siCtrl; ### $P < 0.001$ versus siTREX1. (c) Constitutive activation of IFN- β in TREX1-deficient fibroblasts (SLE, AGS) is further enhanced by siRNA-induced knockdown of RPA70 (siRPA) or Rad51 (siRad51) or both (siRPA + siRad51). This is suppressed by additional knockdown of cGAS (siGAS). Shown are the means of one experiment run in triplicates out of two independent experiments. Error bars, s.d. * $P < 0.001$ versus siCtrl. # $P < 0.001$ versus knockdown of RPA70, Rad51 or RPA70 and Rad51, respectively, by analysis of variance followed by Tukey's *post hoc* test. (d) Repair kinetics of CPDs (left) and DSBs (right) in response to solar-simulated radiation (SSR). Means and s.e.m. of at least three independent experiments for each patient and wild-type control cell lines (WT, $n = 5$). * $P < 0.05$ (LE1, LE2) and ** $P < 0.01$ (AGS1, AGS2) immediately after ultraviolet exposure for CPDs, * $P < 0.05$ (LE1, LE2) and ** $P < 0.01$ (AGS1, AGS2) at 6 h for DSBs. Although TREX1-deficient cells react more sensitive to SSR than WT cells, both DNA lesions are efficiently repaired within 24 h post irradiation. (e) *IFNB* upregulation in patient fibroblasts challenged with poly(I:C) and ultraviolet C irradiation. (WT, $n = 2$). Means and s.e.m. of five independent experiments. * $P < 0.05$; ** $P < 0.01$; *** $P < 0.001$ versus WT. * $P < 0.05$ (AGS2); ** $P < 0.01$ (LE1); *** $P < 0.001$ (LE2, AGS1) for poly(I:C) versus poly(I:C) plus ultraviolet C. Mann-Whitney *U*-test.

repaired in patient and wild-type fibroblasts (Fig. 6d). Thus, TREX1-deficient cells are proficient in pathways of nucleotide excision repair and DNA double-strand break repair.

Like fibroblasts of AGS patients with RNase H2 or SAMHD1 deficiency^{19,20}, TREX1-deficient patient cell exhibit constitutive activation of type I IFN signalling. We, therefore, hypothesized that a cell intrinsic activation of ISGs could render TREX1-deficient cells more sensitive to IFN-dependent stimuli³⁸. To further explore this, we investigated *IFNB* expression in fibroblasts challenged with poly(I:C), a synthetic dsRNA and viral mimic. TREX1-deficient cells responded with a stronger upregulation of *IFNB* than wild-type cells (Fig. 6e). This effect was even more pronounced in cells additionally exposed to environmental genotoxic stress in the form of ultraviolet light, a well-known trigger of SLE flares, suggesting that ultraviolet light could promote type I IFN activation in TREX1-deficient cells by enhancing formation of ssDNA byproducts resulting from repair of DNA photodamage.

Discussion

In this study, we delineate a role of the ssDNA-binding capacity of RPA and Rad51 in the protection of the cytosolic compartment from self DNA emanating from nuclear DNA metabolism. Cells are constantly exposed to genotoxic influences derived from endogenous metabolic byproducts or environmental exposures resulting in tens of thousands of DNA lesions per cell each day, most of which are immediately repaired by DNA repair mechanisms with remarkable efficiency². Nucleotide excision repair, which removes bulky helix-distorting DNA lesions such as ultraviolet light-induced CPDs as well as oxidative DNA lesions, results in the excision of short ssDNA byproducts^{39,40}. Consequently, the cell is challenged by an enormous load of DNA metabolites that need to be properly disposed of to avoid activation of an immune response through recognition by innate immune DNA sensors. While the byproducts of DNA repair are thought to be degraded by nucleases, their intracellular fate remains poorly understood.

The ssDNA-binding proteins RPA and Rad51 play essential roles in pathways of DNA replication, recombination and repair and are abundantly expressed in the nucleus. RPA is a heterotrimeric complex composed of the RPA70, RPA32 and RPA14 subunits, which binds to ssDNA through multiple oligonucleotide/oligosaccharide-binding fold domains²¹. Rad51 on the other hand forms nucleoprotein filaments consisting of multiple ssDNA-bound Rad51 molecules²². RPA participates in DNA replication by enhancing the assembly of DNA polymerases. In addition, both RPA and Rad51 are mobilized to sites of DNA damage, where they protect ssDNA stretches from nucleolytic damage and coordinate the recruitment and exchange of processing factors of a number of DNA repair pathways, in particular during nucleotide excision repair and homologous recombination repair^{41,42}.

Short DNA fragments microinjected into living cells were shown to move between the nucleus and the cytoplasm^{43,44} suggesting that they are either actively exported/imported or freely diffusing through the nuclear pore complexes. Indeed, we demonstrate that short ssDNA microinjected into living cells traverses the nuclear membrane in both directions, but is preferentially drawn into the nucleus. This is illustrated by the observation that ssDNA molecules oozing out from the microinjected nucleus of a binuclear cell are taken up by the non-injected nucleus of the same cell. Nuclear retention of ssDNA is mediated by RPA and Rad51, which bind ssDNA with high affinity. Thus, depletion of RPA and Rad51 causes enhanced cytosolic leakage of exogenous ssDNA microinjected into the

nucleus, while endogenous ssDNA accumulating in TREX1-deficient patient cells is bound by RPA and Rad51 as shown by an increased fraction of ssDNA-bound RPA not associated with chromatin as well as enhanced formation of Rad51 nucleoprotein filaments in the absence of exogenous genotoxic stress. Intriguingly, depletion of RPA and Rad51 in HeLa cells is sufficient to induce type I IFN activation in a cGAS-dependent manner indicating that ssDNA that has escaped the nuclear compartment is recognized by the cytosolic DNA sensor cGAS. Moreover, constitutive type I IFN activation in TREX1-deficient patient cells is further augmented by depletion of RPA and Rad51 suggesting that TREX1 acts in concert with RPA and Rad51 to guard the cytosol from nuclear self DNA.

TREX1 is targeted to the ER within the perinuclear region, which is mediated by a C-terminal hydrophobic domain that is not required for catalytic activity. Notably, C-terminal deletion mutations that impede ER targeting of TREX1 cause the autoimmune disorders RVCL and SLE^{7,8} underpinning a pivotal role of the subcellular localization of TREX1. Indeed, we demonstrate that TREX1 is a tail-anchored protein that integrates within the ER membrane and the outer nuclear membrane via the C-terminal hydrophobic domain with the nuclease domain facing the cytosol. Thus, TREX1 functions as a sentinel nuclease patrolling the border of the nuclear compartment to ensure immediate degradation of ssDNA metabolites leaking out of the nucleus before they can be accessed by the cytosolic DNA sensing machinery.

Recognition of DNA damage by RPA-ssDNA complex formation constitutes a key signal in the activation of ATR kinase-dependent cell cycle checkpoint signalling to protect and repair stalled replication forks³². Notably, an excess of ssDNA caused by unscheduled origin firing was recently shown to exhaust the nuclear pool of RPA accelerating replication fork breakage³³. Likewise, Rad51 recruitment to replication forks is a prerequisite for DNA damage tolerance pathways such as replicative repair of single-strand DNA lesions and replication fork reversal^{34,35}. Hence, augmented binding of ssDNA to RPA and Rad51 in TREX1-deficient cells could promote exhaustion of the nuclear ssDNA-binding capacity leading to chronic checkpoint activation and replication stress through unscheduled engagement of DNA replication/repair pathways. Consistent with this, TREX1-deficient patient fibroblasts exhibit chronic low-level single-strand DNA damage as indicated by an increased pan-nuclear H2AX phosphorylation, checkpoint signalling and a p53-dependent DNA damage response leading to senescence.

A direct role of TREX1 in DNA repair is largely excluded by its cytosolic location and the observation that TREX1-deficient fibroblasts proficiently repair CPDs and DNA double-strand breaks. Consequently, efficient DNA repair in TREX1-deficient cells enhances nuclear formation of ssDNA fragments further contributing to exhaustion of RPA and Rad51. ssDNA that has leaked into the cytosol and is not removed by TREX1 then act as danger-associated molecular pattern (Supplementary Fig. 11). Interestingly, DNA containing 8-oxoguanine, the most common oxidative DNA lesion, was shown to act as a damage-associated molecular pattern⁴⁵, further linking the DNA damage response to innate immune activation.

Autoimmunity in patients with AGS and SLE is characterized by activation of type I IFN signalling^{46–50}. In agreement with this, we demonstrate induction of ISGs in TREX1-deficient fibroblasts besides upregulation of DNA damage response genes. Notably, ISG activation occurred in cultured primary patient fibroblasts not exposed to type I IFN-secreting immune cells confirming a cell autonomous mechanism underlying innate immune activation. Interestingly, a STING/TBK1/IRF3-dependent ISG induction in *Trex1*^{-/-} MEFs is associated with increased

lysosomal biogenesis⁵¹, a phenotype typically observed in senescent cells. Moreover, we demonstrate enhanced *IFNB* upregulation in patient cells in response to poly(I:C) and ultraviolet indicating that constitutive ISG upregulation has a priming effect that renders cells more sensitive to type I IFN-dependent stimuli³⁸. Sunlight, a common trigger of SLE flares, induces primarily CPDs, which are repaired by nucleotide excision repair. Thus, ultraviolet light could create a vicious cycle that fuels and sustains autoimmunity in TREX1 deficiency (Supplementary Fig. 11). Chronic low-level DNA damage and enhanced sensitivity to genotoxic stress also suggest that patients with *TREX1* mutations may have an increased cancer risk, like patients with *SAMHD1* mutations⁵². Moreover, *Trex1*^{-/-} mice were reported to develop carcinogen-induced skin tumours in a STING-dependent manner⁵³. It is of note, in this context, that lupus patient LE1 developed two independent malignancies and a precancerous lesion (Supplementary Note 1).

TREX1 most likely guards the cytosol against ssDNA of any source including viral DNA. *Trex1*^{-/-} MEFs were reported to accumulate ssDNA derived from retroelements¹³, although an increased retroelement activity could not be observed in macrophages or dendritic cells of *Trex1*^{-/-} mice⁵³. On the other hand, TREX1 was shown to facilitate HIV-1 infection by degrading non-productive reverse transcripts of the HIV-1 RNA genome, thereby suppressing a STING-dependent antiviral response⁵⁴. However, as an increased retroelement activity does not explain chronic DNA damage signalling observed in TREX1-deficient patient cells, the pathogenetic role of retroelement-derived DNA in human TREX1 deficiency remains unclear.

Our findings reveal a molecular framework in which the exonuclease TREX1 and the DNA replication and repair factors RPA and Rad51 act together in the disposal of nuclear DNA waste. Interestingly, the physiological role of the TREX1 homologue TREX2, which lacks the transmembrane domain and is expressed in the nucleus, is unknown⁴. It is therefore tempting to speculate that TREX2 might function in the degradation of such DNA metabolites within the nucleus. Further studies are required to test this idea. In conclusion, our findings establish an unanticipated role of the nuclear ssDNA-binding capacity of RPA and Rad51 as an innate defence against self DNA and provide novel mechanistic insight into pathways underlying nucleic acid-driven autoinflammation and autoimmunity.

Methods

Cell lines and plasmids. HeLa cells (ATCC), HEK293T cells (ATCC) and fibroblasts were cultured in DMEM supplemented with 10% FCS, 2 mM L-glutamine and 1% antibiotics-antimycotics. Passage-matched (passages 4–11) cells were used in all experiments. Human primary fibroblasts were derived from skin biopsies with written informed consent from patients or their parents. The study was approved by the ethics committee of the Medical Faculty, TU Dresden. The human TREX1-cDNA was cloned into pEGFP-C1 (GFP-TREX1) and pEGFP-N1 (TREX1-GFP). GFP was replaced with mCherry or YFP using *AgeI* and *BsrGI*. Mutations were introduced by site-directed mutagenesis (QuikChange Lightning, Agilent) or cDNA cloning from patient cells. FLAG-TREX1-glyc constructs were cloned into pCDNA3 by introducing an N-terminal FLAG tag and a fragment coding for the first 19 amino acids of bovine opsin containing two N-linked glycosylation sites (NH₂-MNGTEGPNFYVPPSNKTVTD-COOH, glycosylation sites are underlined)⁵⁵ to the C terminus of wild-type or mutant TREX1. All constructs were verified by sequencing.

Fluorescence protection assay. Fluorescence protection assay was performed as follows³⁰. Briefly, HeLa cells were grown on chamber slides (Lab-Tek II, Nalge-Nunc) and transfected with 120 ng of each GFP-TREX1 and TREX1-mCherry plasmids using FuGENE HD (Roche). Cells were washed with PBS 48 h post transfection and placed on a confocal microscope stage. After taking the first image (pre-permeabilization state), 0.03% Triton X-100 in PBS was added for 30 s and a second image was taken to capture the post-permeabilization state. Following three washes with PBS, 50 µg ml⁻¹ proteinase K was added and the disappearance of the fluorescence signal was documented in consecutive images taken at 30 s intervals. Microscopy was carried out on a Leica TCS SP5 microscope using a × 40 1.25–0.75

oil objective. For the detection of GFP and mCherry, an argon multiline laser (excitation 488 nm; emission 498–584 nm) and a HeNe laser (excitation 594 nm; emission 605–700 nm), respectively, were used.

Glycosylation reporter assay. Templates for *in vitro* transcription/translation were generated by PCR amplification from FLAG-TREX1-glyc plasmids using a T7 promoter-containing sense primer. FLAG-TREX1-glyc proteins were generated using the TnT Quick Coupled Transcription/Translation System (Promega) either in absence or presence of 2 µl microsomal membranes. One aliquot of each reaction was treated with endoglycosidase H for 1 h at 37 °C before SDS-PAGE and western blot using anti-FLAG antibody (Sigma).

Cell proliferation and cell cycle analysis. Fibroblasts were seeded at a density of 2×10^5 cells per flask and counted at indicated time points using a Neubauer chamber. For DNA content analysis, fibroblasts were synchronized by serum starvation for 24 h. At the indicated time points after cultivation in complete growth medium, cells were collected, fixed and stained with propidium iodide. For BrdU labelling, synchronized cells were released at a ratio of 1:4 into complete growth medium containing 10 µM BrdU (BrdU Flow Kit, BD Pharmingen) and stained with 7-aminoactinomycin D (7-AAD) at 24 and 48 h of cultivation. For staining of p21 and γH2AX, trypsinized fibroblasts were fixed in methanol (–20 °C), permeabilized with 0.1% Tween and blocked in 1% BSA. For staining of pATM, cells were fixed in 4% formaldehyde and permeabilized with 0.1% saponin. Cells were then incubated with anti-p21 (clone EA10, Abcam; 1:10), anti-γH2AX (Ser139, clone 2F3, Novus Biologicals; 1:500) or anti-pATM (Ser1981, abcam; 1:500) followed by incubation with Alexa Fluor 488-conjugated goat-anti-mouse-IgG (Molecular Probes). Flow cytometry was performed on a FACSCalibur (Becton Dickinson).

RNA interference. HeLa cells were transfected with TREX1 siRNA (s229446), RPA70 siRNA 1 (s12127), RAD51 siRNA 1 (s11734), STING siRNA (s50644), cGAS siRNA (s41748) and control siRNA (Negative Control #1 siRNA) using Oligofectamine (Invitrogen). siRNAs were from Ambion. Lysates were prepared 72 h after transfection for western blot analysis and IFN-β reporter assay (Supplementary Methods). Images have been cropped for presentation. Full-size images are presented in Supplementary Fig. 12.

Ultraviolet exposure. For determination of DNA repair kinetics, fibroblasts were grown on coverslips, washed with PBS and exposed to solar-simulated ultraviolet radiation using an Arimed B lamp at a radiation dosage of 20 J m⁻² (DNA double-strand breaks) or 100 J m⁻² (CPDs). At the indicated time points post irradiation, cells were fixed and stained for DSBs or CPDs. *IFNB* expression was determined in fibroblasts grown in six-well plates following exposure to ultraviolet C-light (254 nm, Hg-low pressure lamp) at a radiation dosage of 30 J m⁻². Before ultraviolet C irradiation, cells were either left untreated or incubated with 100 µg ml⁻¹ poly(I:C) (InvivoGen) for 3 h. Slides were then washed with PBS and fresh medium added. 4 h post irradiation, cells were processed for RNA isolation.

Quantitative real-time reverse transcription-PCR. Total RNA from fibroblasts was extracted with the RNeasy Mini Kit (Qiagen) followed by DNase I digestion. Expression of *IFNB* and ISGs was determined by quantitative real-time reverse transcription-PCR using Taqman Universal PCR Master Mix (Applied Biosystems) on an ABI7300 and normalized to GAPDH expression. Each experiment was run triplicates. *IFI44L*, *IFIT1*, *ISG15* and *RSAD2* gene expression was determined using a pre-designed TaqMan Gene Expression Assay (Applied Biosystems). For oligonucleotides (Eurofins MWG Operon) used for quantitative real-time reverse transcription-PCR see Supplementary Table 2.

Statistical analysis. Statistical significance was determined by two-tailed Student's *t*-test, Mann-Whitney *U*-test or analysis of variance followed by Tukey's *post hoc* test. Values of *P* < 0.05 were considered statistically significant. Data are represented as means ± s.d. or s.e.m. as indicated.

Data availability. RNA sequencing data generated in this study were submitted to the Gene Expression Omnibus (GEO) database under accession number GSE59233.

References

- Atianand, M. K. & Fitzgerald, K. A. Molecular basis of DNA recognition in the immune system. *J. Immunol.* **190**, 1911–1918 (2013).
- Lindahl, T. & Wood, R. D. Quality control by DNA repair. *Science* **286**, 1897–1905 (1999).
- Hoss, M. *et al.* A human DNA editing enzyme homologous to the *Escherichia coli* DnaQ/MutD protein. *EMBO J.* **18**, 3868–3875 (1999).
- Mazur, D. J. & Perrino, F. W. Identification and expression of the TREX1 and TREX2 cDNA sequences encoding mammalian 3'→5' exonucleases. *J. Biol. Chem.* **274**, 19655–19660 (1999).

5. Crow, Y. J. *et al.* Mutations in the gene encoding the 3'-5' DNA exonuclease TREX1 cause Aicardi-Goutieres syndrome at the AGS1 locus. *Nat. Genet.* **38**, 917–920 (2006).
6. Rice, G. *et al.* Heterozygous mutations in TREX1 cause familial chilblain lupus and dominant Aicardi-Goutieres syndrome. *Am. J. Hum. Genet.* **80**, 811–815 (2007).
7. Richards, A. *et al.* C-terminal truncations in human 3'-5' DNA exonuclease TREX1 cause autosomal dominant retinal vasculopathy with cerebral leukodystrophy. *Nat. Genet.* **39**, 1068–1070 (2007).
8. Lee-Kirsch, M. A. *et al.* Mutations in the gene encoding the 3'-5' DNA exonuclease TREX1 are associated with systemic lupus erythematosus. *Nat. Genet.* **39**, 1065–1067 (2007).
9. Namjou, B. *et al.* Evaluation of the TREX1 gene in a large multi-ancestral lupus cohort. *Genes Immun.* **12**, 270–279 (2011).
10. Crow, Y. J. *et al.* Mutations in genes encoding ribonuclease H2 subunits cause Aicardi-Goutieres syndrome and mimic congenital viral brain infection. *Nat. Genet.* **38**, 910–916 (2006).
11. Rice, G. I. *et al.* Mutations involved in Aicardi-Goutieres syndrome implicate SAMHD1 as regulator of the innate immune response. *Nat. Genet.* **41**, 829–832 (2009).
12. Rice, G. I. *et al.* Mutations in ADARI cause Aicardi-Goutieres syndrome associated with a type I interferon signature. *Nat. Genet.* **44**, 1243–1248 (2012).
13. Stetson, D. B., Ko, J. S., Heidmann, T. & Medzhitov, R. Trex1 prevents cell-intrinsic initiation of autoimmunity. *Cell* **134**, 587–598 (2008).
14. Gall, A. *et al.* Autoimmunity initiates in nonhematopoietic cells and progresses via lymphocytes in an interferon-dependent autoimmune disease. *Immunity* **36**, 120–131 (2012).
15. Ablasser, A. *et al.* TREX1 deficiency triggers cell-autonomous immunity in a cGAS-dependent manner. *J. Immunol.* **192**, 5993–5997 (2014).
16. Gray, E. E., Treuting, P. M., Woodward, J. J. & Stetson, D. B. Cutting edge: cGAS is required for lethal autoimmune disease in the Trex1-deficient mouse model of Aicardi-Goutieres syndrome. *J. Immunol.* **195**, 1939–1943 (2015).
17. Gao, D. *et al.* Activation of cyclic GMP-AMP synthase by self-DNA causes autoimmune diseases. *Proc. Natl Acad. Sci. USA* **112**, E5699–E5705 (2015).
18. Yang, Y. G., Lindahl, T. & Barnes, D. E. Trex1 exonuclease degrades ssDNA to prevent chronic checkpoint activation and autoimmune disease. *Cell* **131**, 873–886 (2007).
19. Gunther, C. *et al.* Defective removal of ribonucleotides from DNA promotes systemic autoimmunity. *J. Clin. Invest.* **125**, 413–424 (2015).
20. Kretschmer, S. *et al.* SAMHD1 prevents autoimmunity by maintaining genome stability. *Ann. Rheum. Dis.* **74**, e17 (2015).
21. Bochkarev, A. & Bochkareva, E. From RPA to BRCA2: lessons from single-stranded DNA binding by the OB-fold. *Curr. Opin. Struct. Biol.* **14**, 36–42 (2004).
22. Mine, J. *et al.* Real-time measurements of the nucleation, growth and dissociation of single Rad51-DNA nucleoprotein filaments. *Nucleic Acids Res.* **35**, 7171–7187 (2007).
23. Civril, F. *et al.* Structural mechanism of cytosolic DNA sensing by cGAS. *Nature* **498**, 332–337 (2013).
24. Gao, D. *et al.* Cyclic GMP-AMP synthase is an innate immune sensor of HIV and other retroviruses. *Science* **341**, 903–906 (2013).
25. Herzner, A. M. *et al.* Sequence-specific activation of the DNA sensor cGAS by Y-form DNA structures as found in primary HIV-1 cDNA. *Nat. Immunol.* **16**, 1025–1033 (2015).
26. Fujimoto, M. *et al.* RPA assists HSF1 access to nucleosomal DNA by recruiting histone chaperone FACT. *Mol. Cell* **48**, 182–194 (2012).
27. Peng, G. *et al.* Genome-wide transcriptome profiling of homologous recombination DNA repair. *Nat. Commun.* **5**, 3361 (2014).
28. Meindl, A. *et al.* Germline mutations in breast and ovarian cancer pedigrees establish RAD51C as a human cancer susceptibility gene. *Nat. Genet.* **42**, 410–414 (2010).
29. Sestili, P. The fast-halo assay for the assessment of DNA damage at the single-cell level. *Methods Mol. Biol.* **521**, 517–533 (2009).
30. Lorenz, H., Hailey, D. W. & Lippincott-Schwartz, J. Fluorescence protease protection of GFP chimeras to reveal protein topology and subcellular localization. *Nat. Methods* **3**, 205–210 (2006).
31. Snapp, E. L. *et al.* Formation of stacked ER cisternae by low affinity protein interactions. *J. Cell Biol.* **163**, 257–269 (2003).
32. Zou, L. & Elledge, S. J. Sensing DNA damage through ATRIP recognition of RPA-ssDNA complexes. *Science* **300**, 1542–1548 (2003).
33. Toledo, L. I. *et al.* ATR prohibits replication catastrophe by preventing global exhaustion of RPA. *Cell* **155**, 1088–1103 (2013).
34. Gonzalez-Prieto, R., Munoz-Cabello, A. M., Cabello-Lobato, M. J. & Prado, F. Rad51 replication fork recruitment is required for DNA damage tolerance. *EMBO J.* **32**, 1307–1321 (2013).
35. Zellweger, R. *et al.* Rad51-mediated replication fork reversal is a global response to genotoxic treatments in human cells. *J. Cell Biol.* **208**, 563–579 (2015).
36. Reijns, M. A. *et al.* Enzymatic removal of ribonucleotides from DNA is essential for mammalian genome integrity and development. *Cell* **149**, 1008–1022 (2012).
37. Hiller, B. *et al.* Mammalian RNase H2 removes ribonucleotides from DNA to maintain genome integrity. *J. Exp. Med.* **209**, 1419–1426 (2012).
38. Taniguchi, T. & Takaoka, A. A weak signal for strong responses: interferon-alpha/beta revisited. *Nat. Rev. Mol. Cell Biol.* **2**, 378–386 (2001).
39. Lindahl, T., Karran, P. & Wood, R. D. DNA excision repair pathways. *Curr. Opin. Genet. Dev.* **7**, 158–169 (1997).
40. Guo, J., Hanawalt, P. C. & Spivak, G. Comet-FISH with strand-specific probes reveals transcription-coupled repair of 8-oxoGuanine in human cells. *Nucleic Acids Res.* **41**, 7700–7712 (2013).
41. Marechal, A. & Zou, L. RPA-coated single-stranded DNA as a platform for post-translational modifications in the DNA damage response. *Cell Res.* **25**, 9–23 (2015).
42. Krejci, L., Altmanova, V., Spirek, M. & Zhao, X. Homologous recombination and its regulation. *Nucleic Acids Res.* **40**, 5795–5818 (2012).
43. Lukacs, G. L. *et al.* Size-dependent DNA mobility in cytoplasm and nucleus. *J. Biol. Chem.* **275**, 1625–1629 (2000).
44. Shimizu, N., Kamezaki, F. & Shigematsu, S. Tracking of microinjected DNA in live cells reveals the intracellular behavior and elimination of extrachromosomal genetic material. *Nucleic Acids Res.* **33**, 6296–6307 (2005).
45. Gehrke, N. *et al.* Oxidative damage of DNA confers resistance to cytosolic nuclease TREX1 degradation and potentiates STING-dependent immune sensing. *Immunity* **39**, 482–495 (2013).
46. Lebon, P. *et al.* Intrathecal synthesis of interferon-alpha in infants with progressive familial encephalopathy. *J. Neurol. Sci.* **84**, 201–208 (1988).
47. Ramantani, G. *et al.* Expanding the phenotypic spectrum of lupus erythematosus in Aicardi-Goutieres syndrome. *Arthritis Rheum.* **62**, 1469–1477 (2010).
48. Rice, G. I. *et al.* Assessment of interferon-related biomarkers in Aicardi-Goutieres syndrome associated with mutations in TREX1, RNASEH2A, RNASEH2B, RNASEH2C, SAMHD1, and ADAR: a case-control study. *Lancet Neurol.* **12**, 1159–1169 (2013).
49. Peschke, K. *et al.* Deregulated type I IFN response in TREX1-associated familial chilblain lupus. *J. Invest. Dermatol.* **134**, 1456–1459 (2014).
50. Ronnblom, L., Alm, G. V. & Eloranta, M. L. Type I interferon and lupus. *Curr. Opin. Rheumatol.* **21**, 471–477 (2009).
51. Hasan, M. *et al.* Trex1 regulates lysosomal biogenesis and interferon-independent activation of antiviral genes. *Nat. Immunol.* **14**, 61–71 (2013).
52. Clifford, R. *et al.* SAMHD1 is mutated recurrently in chronic lymphocytic leukemia and is involved in response to DNA damage. *Blood* **123**, 1021–1031 (2014).
53. Ahn, J. *et al.* Inflammation-driven carcinogenesis is mediated through STING. *Nat. Commun.* **5**, 5166 (2014).
54. Yan, N., Regalado-Magdos, A. D., Stiggelbout, B., Lee-Kirsch, M. A. & Lieberman, J. The cytosolic exonuclease TREX1 inhibits the innate immune response to human immunodeficiency virus type 1. *Nat. Immunol.* **11**, 1005–1013 (2010).
55. Colombo, S. F., Longhi, R. & Borgese, N. The role of cytosolic proteins in the insertion of tail-anchored proteins into phospholipid bilayers. *J. Cell Sci.* **122**, 2383–2392 (2009).

Acknowledgements

We thank Kerstin Engel, Susan Hunger and Nick Zimmermann for excellent technical assistance. We thank Fabio Vilardi (University of Heidelberg) for microsomal membranes and Nica Borgese (Institute of Neuroscience, Milan) for b5-ops28 plasmid. We thank Michael Haase, Rayk Behrendt and Axel Roers for helpful discussions. We thank Dimitra Alexopoulou and Andreas Dahl for RNA sequencing. We thank Markus Burkhardt and Jan Pechl for support with raster image correlation spectroscopy data acquisition and analysis. The Light Microscopy Facility and the Deep Sequencing Facility of the Biotechnology Center and the Center for Regenerative Therapies Dresden, TU Dresden, are funded by the Deutsche Forschungsgemeinschaft. This work was supported by grants from the Deutsche Forschungsgemeinschaft (LE 1074/3-1, LE 1074/3-1 and LE 1074/4-1 to M.L.-K.; GU1212/1-1 and GU 1212/1-2 to C.G.), the Bundesministerium für Bildung und Forschung (02S8355 and 02NUK017D to M.C.C.; 02NUK036D to A.R.) and the Friede Springer Stiftung to M.L.-K.

Author contributions

C.W., A.R., W.S., M.C.C., C.G. and M.L.-K. designed experiments and analysed data. C.W., A.R., N.B., W.S., M.S., N.K., M.D.-M., S.K. and T.K. performed experiments. D.W. and K.K. provided patient material and advice. C.W., A.R., M.C.C., C.G. and M.L.-K. wrote the manuscript. M.L.-K. supervised the study.

Additional information

Accession codes: RNA sequencing data generated in this study were submitted to the Gene Expression Omnibus (GEO) database under accession number GSE59233.

Supplementary Information accompanies this paper at <http://www.nature.com/naturecommunications>

Competing financial interests: The authors declare no competing financial interests.

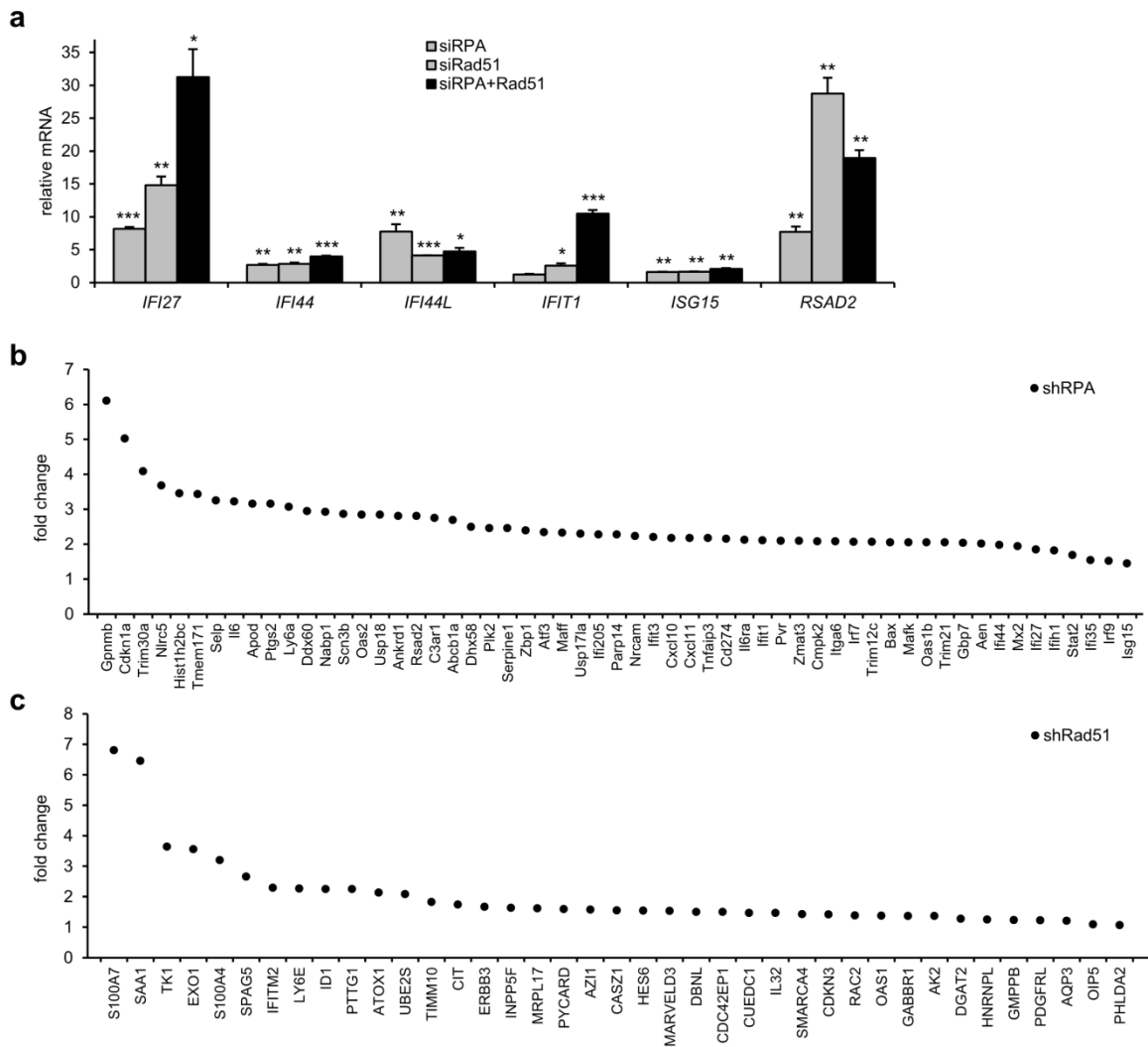
Reprints and permission information is available online at <http://npg.nature.com/reprintsandpermissions/>

How to cite this article: Wolf, C. *et al.* RPA and Rad51 constitute a cell intrinsic mechanism to protect the cytosol from self DNA. *Nat. Commun.* 7:11752 doi: 10.1038/ncomms11752 (2016).

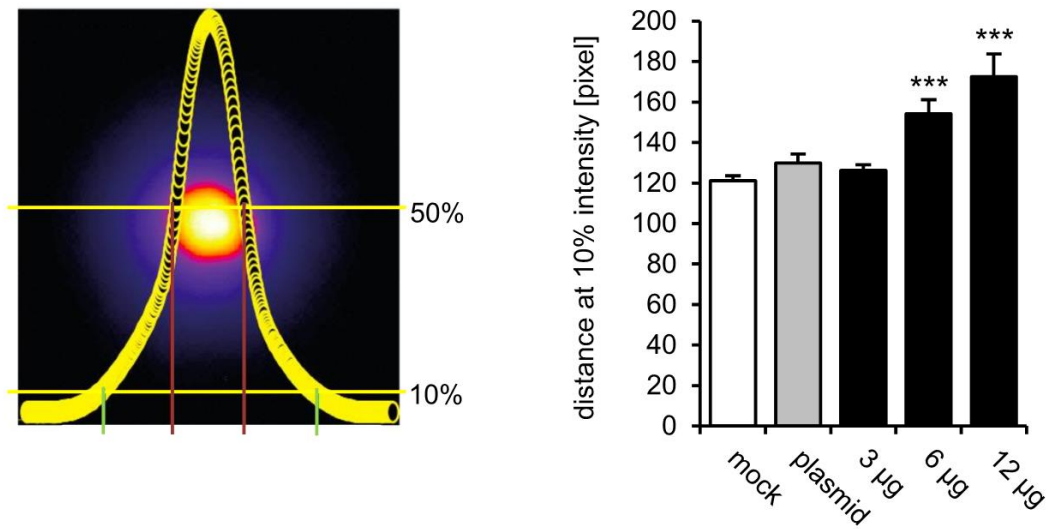


This work is licensed under a Creative Commons Attribution 4.0 International License. The images or other third party material in this article are included in the article's Creative Commons license, unless indicated otherwise in the credit line; if the material is not included under the Creative Commons license, users will need to obtain permission from the license holder to reproduce the material. To view a copy of this license, visit <http://creativecommons.org/licenses/by/4.0/>

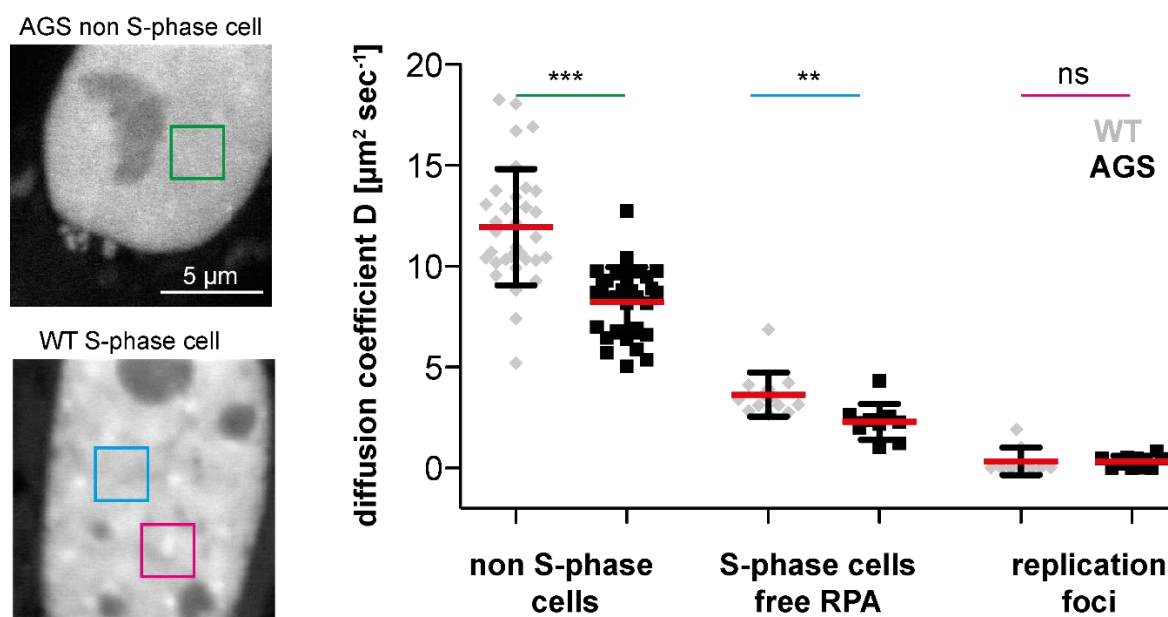
Supplementary Figures



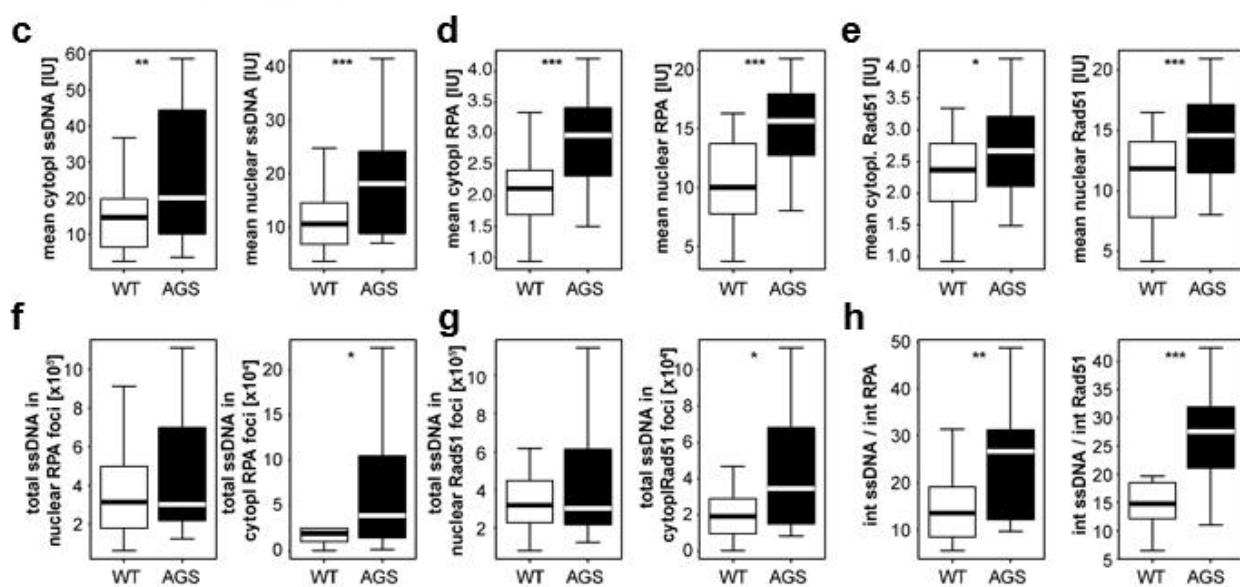
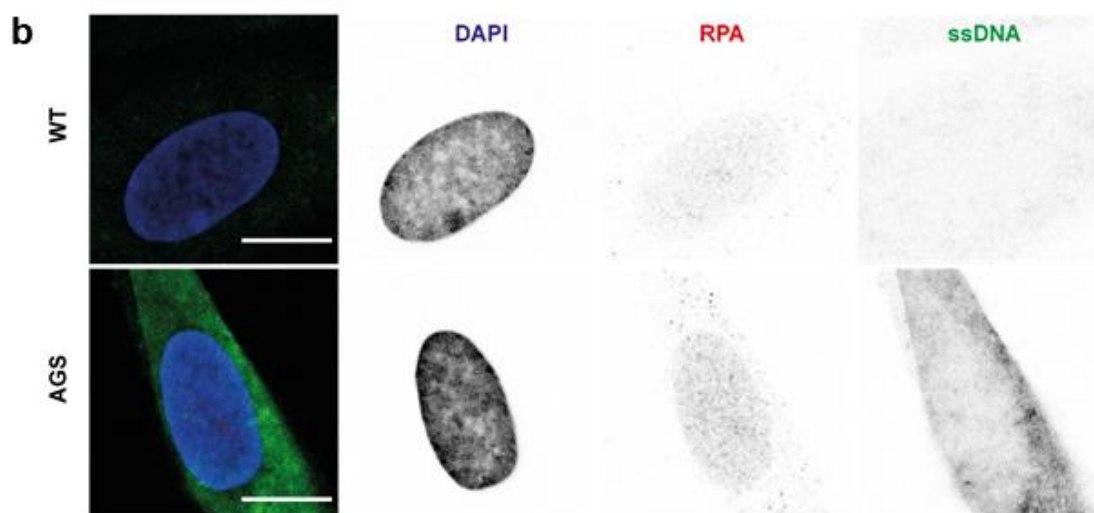
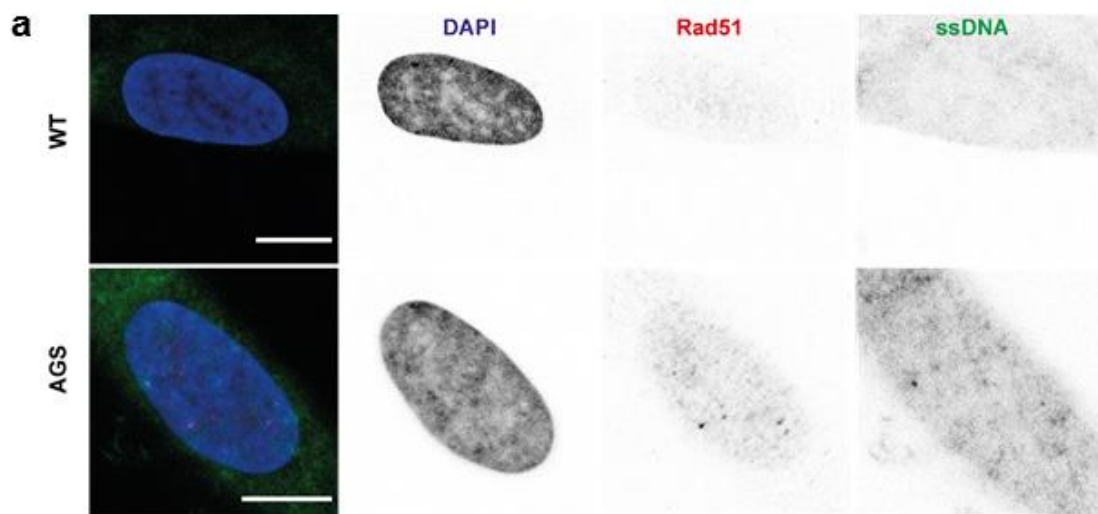
Supplementary Figure 1. Knockdown of RPA and Rad51 leads to ISG induction. (a) siRNA-induced knockdown of RPA70 (siRPA) and Rad51 (siRad51) in HeLa cells leads to induction of the interferon-stimulated genes *IFI27*, *IFI44*, *IFI44L*, *IFIT1*, *ISG15* and *RSAD2*. Shown is the fold-change in gene expression relative to a negative control siRNA. Means and s.e.m. of at least two independent experiments run in triplicate. * $P < 0.05$; ** $P < 0.01$; *** $P < 0.001$. (b, c) Transcriptional signatures of ISGs obtained from MEFs with shRNA-induced knockdown of RPA ($n = 3$) (b) and from human MCF-10A cells with shRNA-induced knockdown of Rad51 ($n = 4$) (c). Shown are the fold changes in ISG expression for each group relative to controls treated with scrambled shRNA ($n = 3$ per group) with an adjusted $P < 0.05$. Transcriptome data were retrieved from the GEO database (accession numbers: GSE38412, GSE54266) and analyzed with GEO2R.



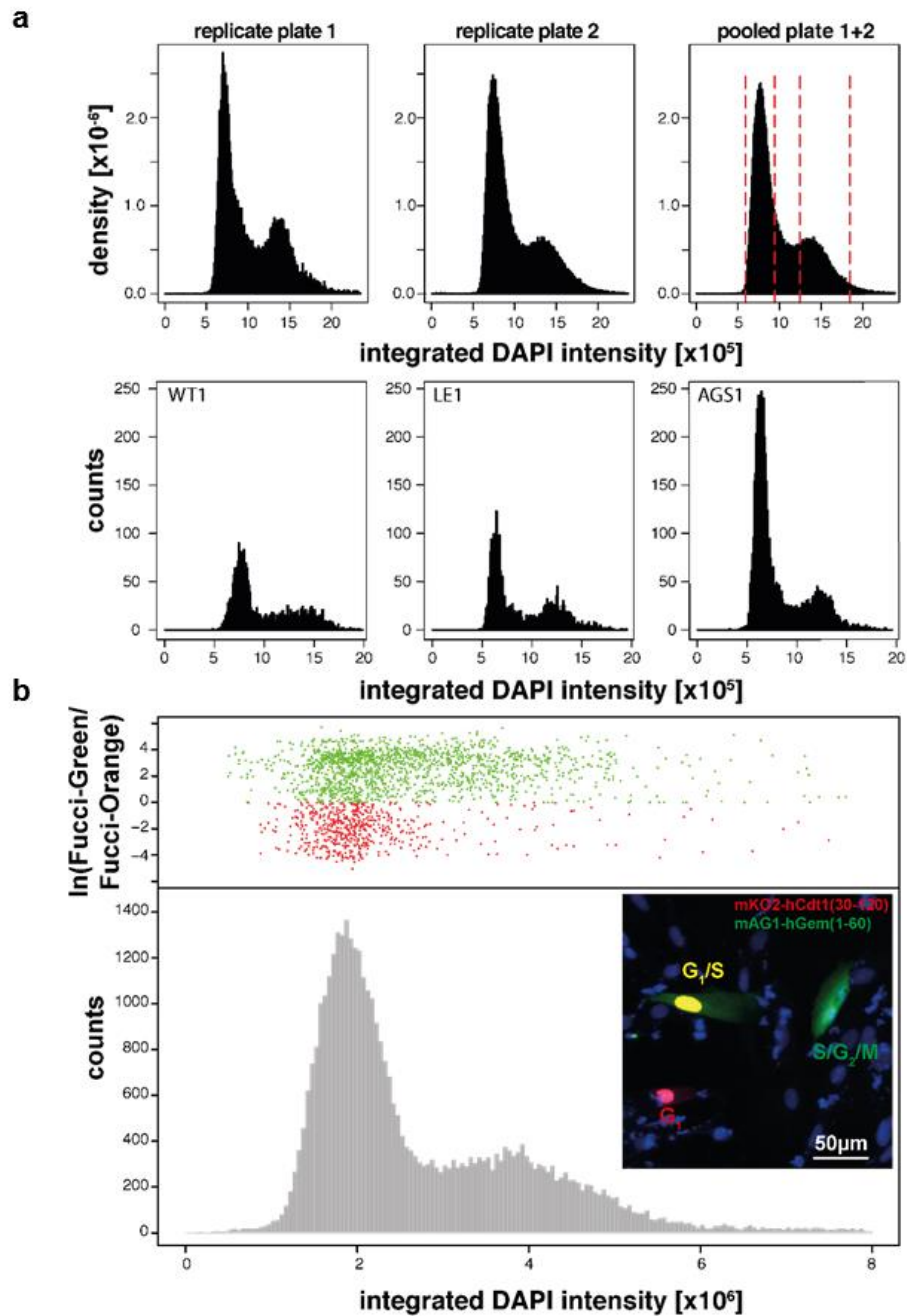
Supplementary Figure 2. Halo assay of fibroblasts transfected with a 45 bp ssDNA oligonucleotide. Schematic of intensity plot used to calculate halo diameters at 10% maximum intensity. Human fibroblasts transfected with increasing amounts of a 45 bp ssDNA oligonucleotide (3, 6, 12 µg) or a 5 kb plasmid (6 µg) show a dose-dependent halo formation. Shown are the means and s.e.m. of two independent experiments run in triplicates. *** $P < 0.001$.



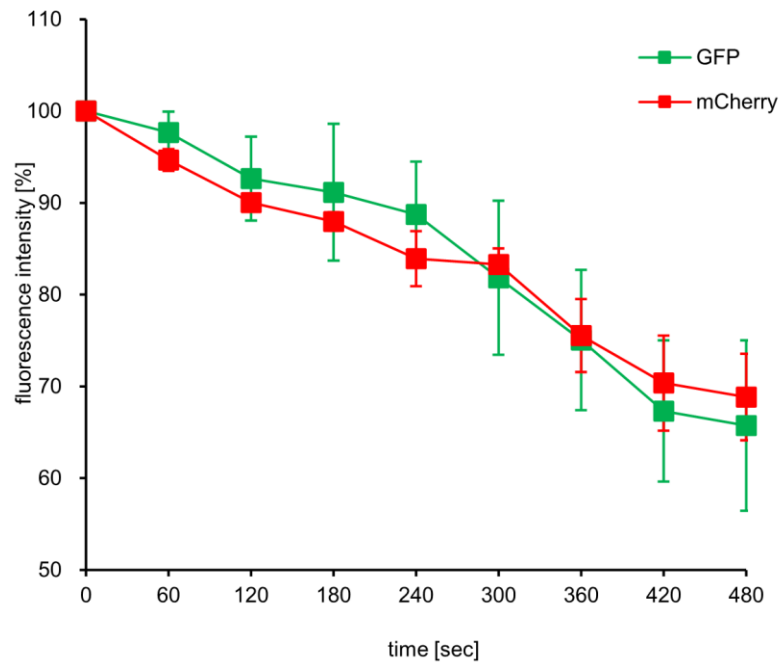
Supplementary Figure 3. Mobility of RPA complexes in living cells measured by raster image correlation spectroscopy (RICS). (a) GFP-RPA32 transfected wild type and AGS patient fibroblasts were analyzed by RICS in three distinct conditions. In non S-phase cells (green), in non focal areas in S-phase cells (cyan) and in replication foci (magenta). (b) Diffusion coefficients obtained from at least 10 cells per sample. While in wild type cells, RPA34-GFP shows a mean diffusion coefficient of $11.9 + 2.8 \mu\text{m}^2 \text{sec}^{-1}$, AGS cells have a reduced diffusion coefficient of $8.2 + 1.7 \mu\text{m}^2 \text{sec}^{-1}$ indicating that RPA is part of a larger complex in AGS cells. Based on the molecular weight, free RPA is expected to have a diffusion coefficient of approximately $30 \mu\text{m}^2 \text{sec}^{-1}$ ³. In S-phase cells, RPA is present in two forms, free RPA and focal RPA engaged in replication. Again the AGS cells exhibit a reduced RPA diffusion ($2.2 + 0.9 \mu\text{m}^2 \text{sec}^{-1}$), consistent with larger complexes, compared to wild type cells ($3.6 + 1.0 \mu\text{m}^2 \text{sec}^{-1}$). This fraction is distinct from the RPA fraction engaged in replication foci that exhibits nearly no mobility in both patients and wild type cells ($0.3 + 0.6$ vs. $0.3 + 0.3 \mu\text{m}^2 \text{sec}^{-1}$). Red bars represent means, whiskers s.d.. *** $P < 0.001$; ** $P < 0.01$; ns, not significant. ANOVA with Bonferroni's multiple comparison test.



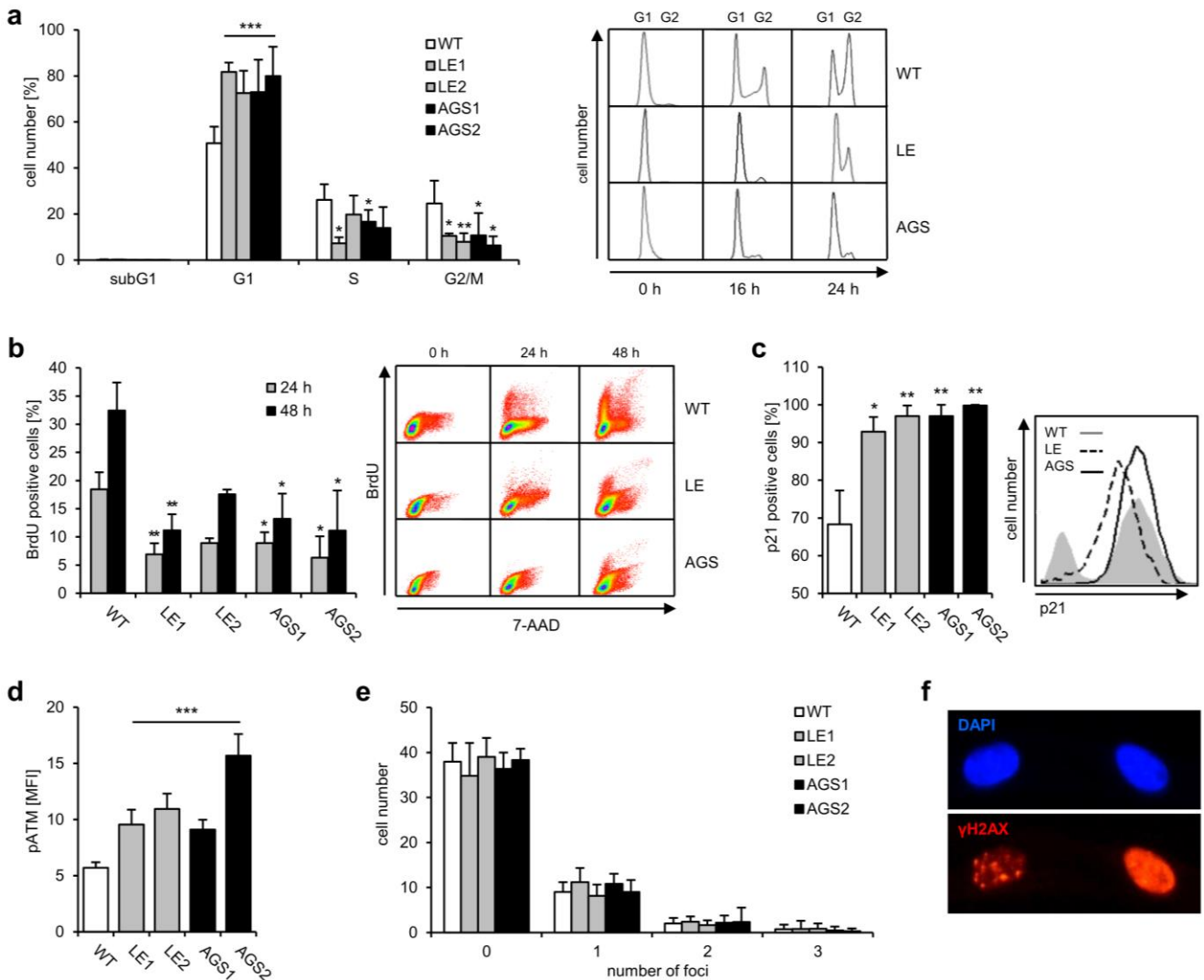
Supplementary Figure 4. Co-staining of ssDNA and RPA or Rad51. (a, b) Confocal mid nuclear sections of wild type (WT) fibroblasts and TREX1-deficient patient fibroblasts (AGS) co-stained for ssDNA (green) and RPA or Rad51, respectively (red). Nuclei are counterstained with DAPI (blue). AGS cells show enhanced levels of ssDNA compared to WT cells, both in the cytoplasm and the nucleus (c). This is accompanied with increased levels of nuclear RPA and Rad51 as well as cytoplasmic RPA and Rad51 (d, e). Increased co-localization between ssDNA and RPA or Rad51, respectively, is detectable in the cytoplasm, but not in the nucleus (f, g). The intensity ratios between ssDNA and RPA or Rad51, respectively, are significantly increased in AGS patient cells indicating an exhaustion of the cellular Rad51 and RPA pools (h). Boxplots represent the 25th to 75th percentile and whiskers the 5th to 95th percentile. Horizontal lines denote means. * $P < 0.1$, ** $P < 0.01$, *** $P < 0.001$, Student's t test.



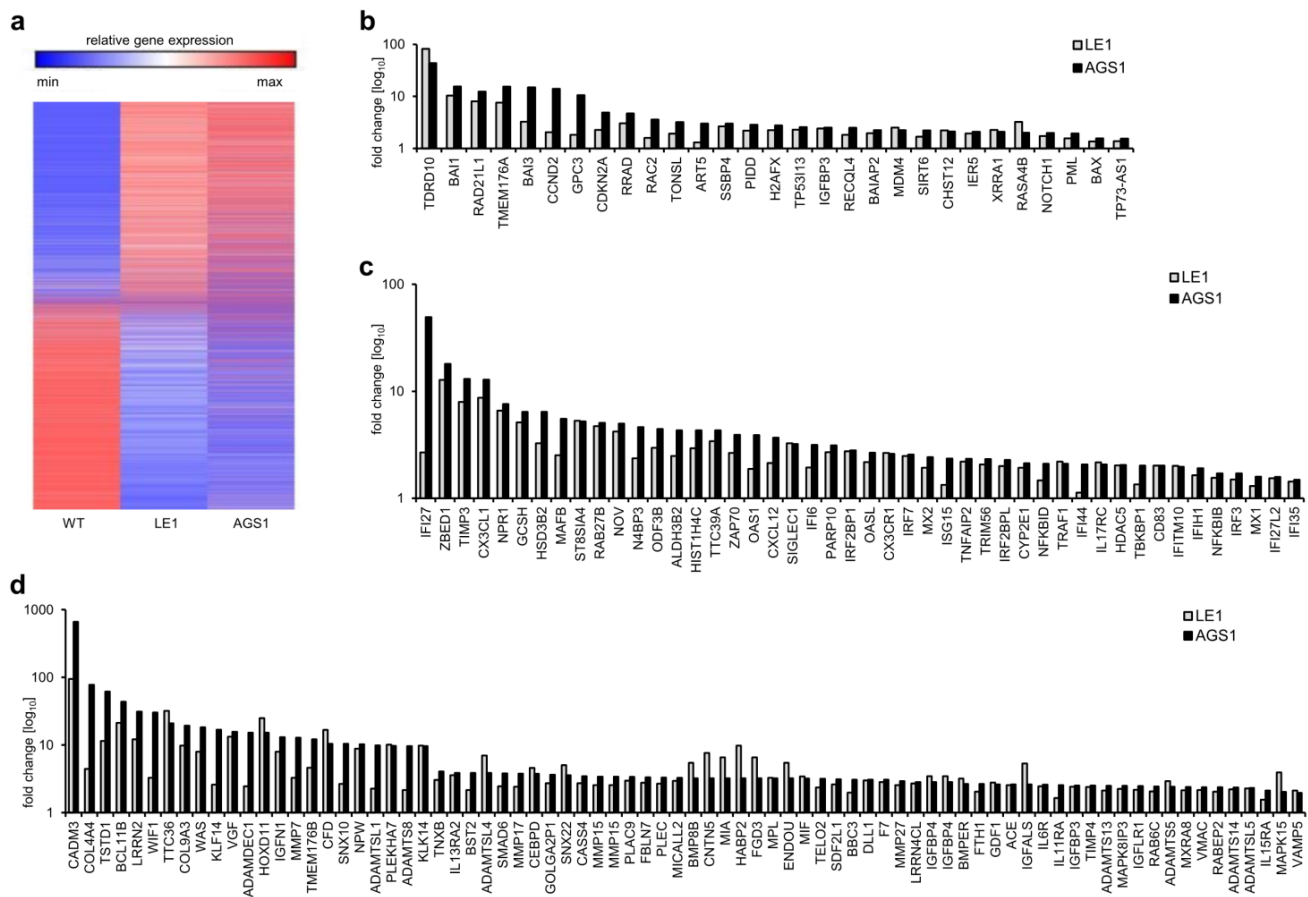
Supplementary Figure 5. Cell cycle analysis by DNA content based on integrated DAPI intensities. (a) Comparison of raw data from two different 96-well plates and the pooled dataset (upper panel) as well as from three cell lines (WT1, LE1, AGS1) obtained from single wells (lower panel) demonstrates a stable cell cycle segmentation with clearly identifiable G_1 and G_2 peaks. (b) To further validate the DAPI-based cell cycle classification, fibroblasts were transfected with the fluorescent ubiquitination-based cell cycle indicators Kusabira-Orange2-tagged Cdt1 and Azami Green1-tagged Geminin. This results in red nuclei if cells are in G_1 and in green cells if cells are in S, G_2 or M phase. The presence of both colors indicate G_1/S transition. The cell cycle distribution based on integrated DAPI intensities (histogram) corresponds to the distribution of red (G_1) and green (S/ G_2 /M) fluorescence measured in the same cells.



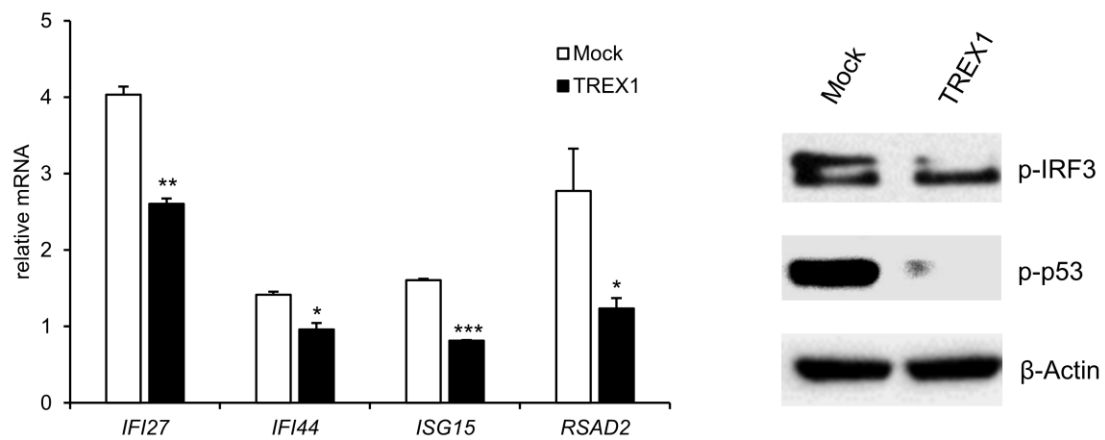
Supplementary Figure 6. Fluorescence intensity decay curves of GFP-TREX1 and TREX1-mCherry. Fluorescence intensities were normalized by setting the highest intensity of each fluorophore to 100%. Shown are mean values and s.d. of triplicate measurements.



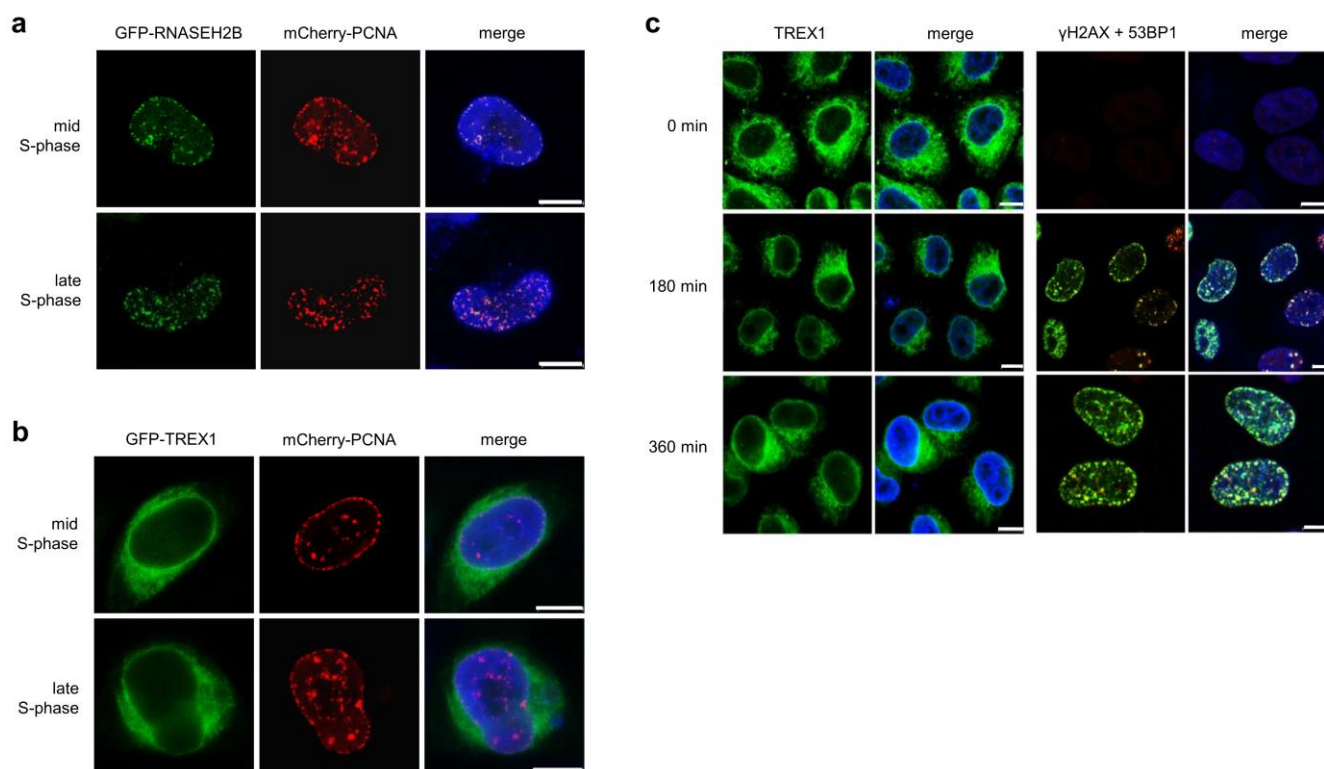
Supplementary Figure 7. Cell cycle delay, DNA damage signaling and checkpoint activation in TREX1-deficient fibroblast. (a) Cell cycle analysis of synchronized fibroblasts 16 h after release into growth medium measured by flow cytometry (left). Representative histograms (right). (b) Quantification of BrdU-positive fibroblasts showing defective G₁/S transition in TREX1-deficient compared to wild type cells (left). Representative scatter plots of patient (LE, AGS) and wild type (WT) cells 24 and 48 h after BrdU-labeling (right). (c, d) Flow cytometry of fibroblasts stained for p21 (c) and pATM (d). (e) Quantification of DNA double-strand breaks determined by counting of γ H2AX and 53BP1-double positive nuclear foci. (f) Confocal image of patient fibroblasts showing a nucleus with pan-nuclear staining next to a nucleus with focal staining of γ H2AX (red). Nuclei counterstained with DAPI (blue). Shown are the means and s.e.m. of two (c), three (a, b, e) or six (d) independent experiments for each patient (LE1, LE2, AGS1, AGS2) and five wild type controls (WT). * $P < 0.05$; ** $P < 0.01$; *** $P < 0.001$.



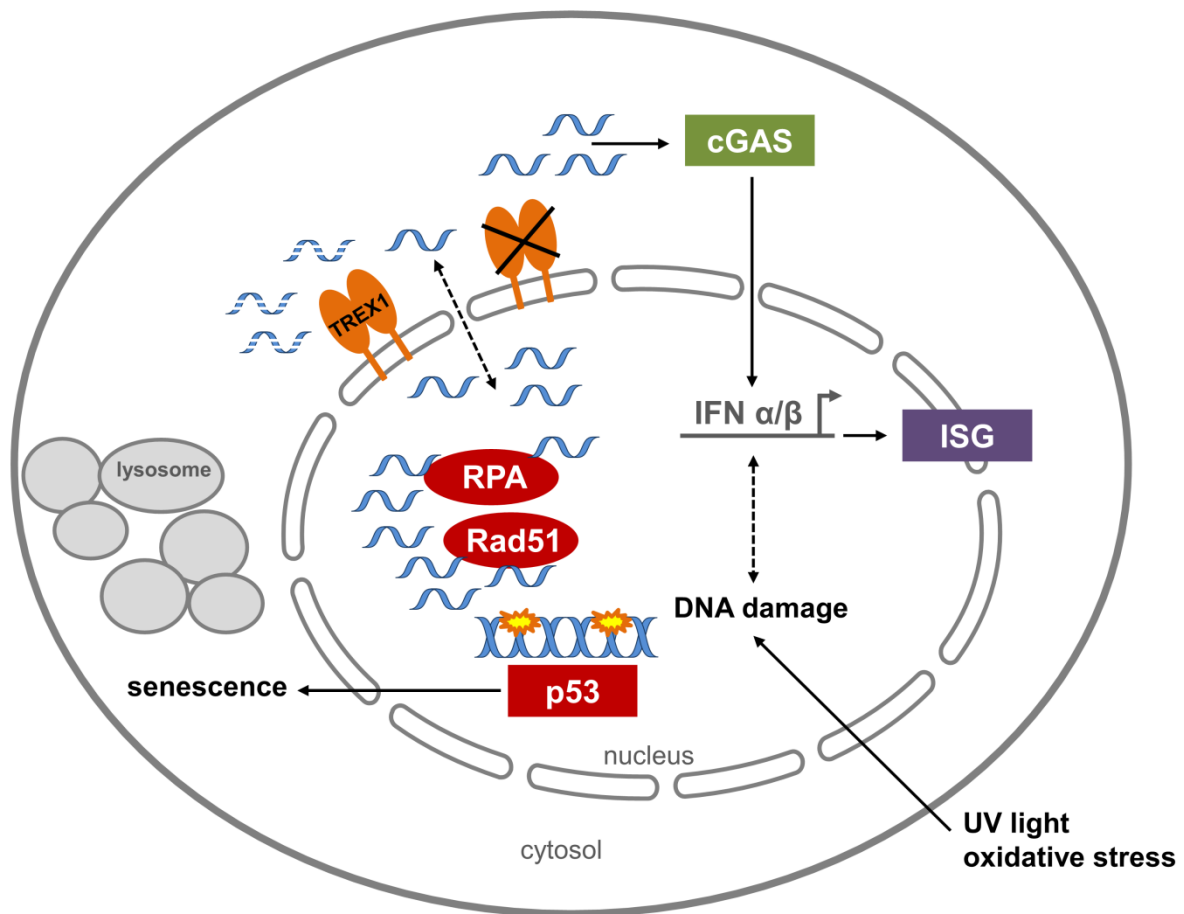
Supplementary Figure 8. Constitutive activation of genes involved in the DNA damage response and of interferon-stimulated genes in TREP1-deficient fibroblasts. (a) Transcriptome analysis of patient fibroblasts (LE1, AGS1) and wild type controls (WT, n = 2, mean). The heat map represents over 9000 hierarchically clustered transcripts displaying up-regulation by a factor of at least two. **(b, c, d)** Fold-changes of the RPKM values of patient fibroblasts (LE1, AGS1) relative to the mean RPKM values of wild type controls (WT, n = 2). Up-regulation of DNA damage response genes (b), interferon-stimulated genes (c) and of genes involved in structural and metabolic changes associated with senescence (d).



Supplementary Figure 9. Rescue of constitutive activation of type I IFN and DNA damage signaling by overexpression of wild type TREX1 in AGS fibroblasts. TREX1-deficient fibroblasts from an AGS patient transiently transfected with wild type TREX1 (TREX1) exhibit decreased expression of interferon-stimulated genes (left) along with reduced levels of phosphorylated IRF3 (p-IRF3) and p53 (p-p53; right) compared to cells transfected with empty vector (Mock). Quantitative RT-PCR data are presented as means and s.e.m. of one representative experiment run in triplicates out of two independent experiments. * $P < 0.05$; *** $P < 0.01$.



Supplementary Figure 10. TREX1 does not associate with nuclear foci during DNA replication or repair. (a, b) GFP-RNASEH2B (green, upper panels), but not GFP-TREX1 (green, lower panels), is recruited to replication foci in S-phase nuclei as shown by co-localization with mCherry-PCNA (red) in HeLa cells. Nuclei are stained with DAPI (blue). Scale bars, 10 μ M. (c) Endogenous TREX1 stained with anti-TREX1 does not associate with DNA damage foci in HeLa cells in response to 6 mM hydroxyurea as shown by immunostaining of γ H2AX (green) and 53BP1 (red). Nuclei are stained with DAPI (blue). Scale bars, 10 μ M.



Supplementary Figure 11. Model depicting the role of TREX1 and the ssDNA-binding proteins RPA and Rad51 in the protection of the cytosol from self DNA. Nucleotide excision repair of DNA lesions induced by UV light or oxidative stress results in formation of short ssDNA fragments. The cytosolic tail-anchored nuclease TREX1 degrades nuclear ssDNA that has leaked into the cytosol. In TREX1-deficiency, ssDNA accumulates both in the cytosol and nucleus. In the cytosol, ssDNA is sensed by the pattern-recognition receptor cGAS resulting in type I IFN-dependent innate immune activation. In the nucleus, enhanced ssDNA-binding to RPA and Rad51 causes RPA and Rad51 exhaustion. This leads to unscheduled engagement DNA replication/repair resulting in replication stress and further DNA damage. Chronic low level DNA damage induces a p53-dependent DNA damage response and senescence, which may further contribute to activation of interferon-stimulated genes (ISG).

Fig. 1e

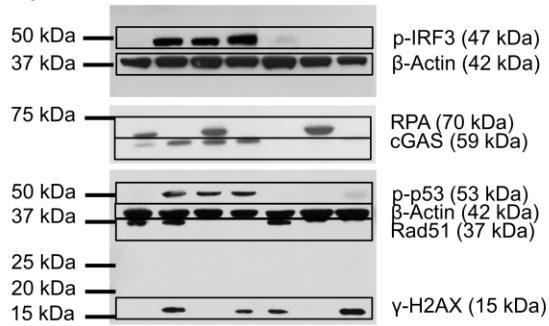


Fig. 3d

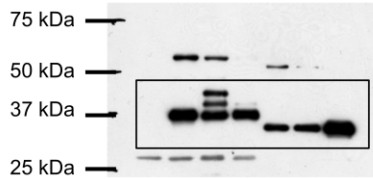


Fig. 6a

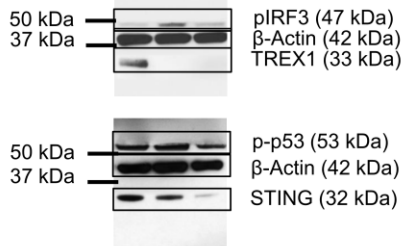
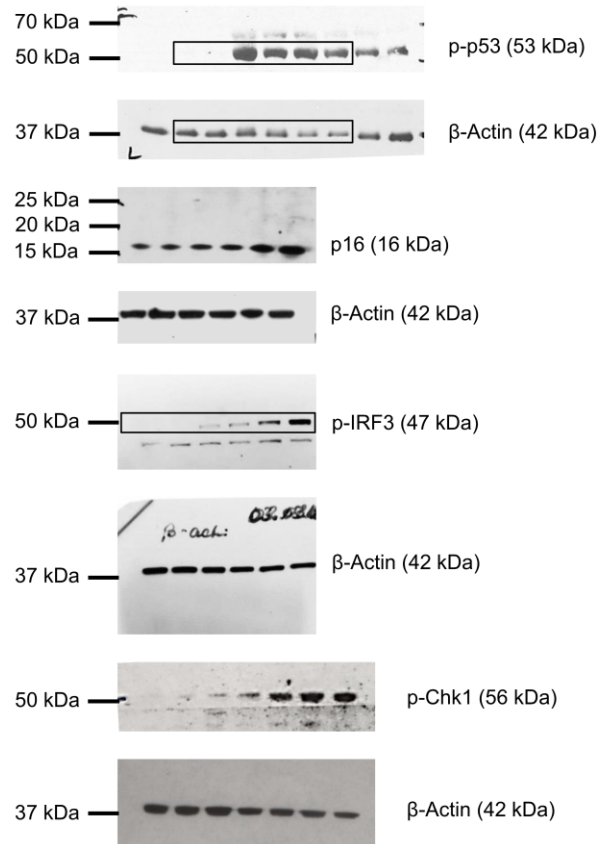


Fig. 5d



Supplementary Figure 12. Uncropped blots.

Supplementary Tables

Supplementary Table 1. Clinical and laboratory findings in 4 unrelated patients with hereditary breast and ovarian cancer syndrome due to heterozygous germ line mutation in *RAD51C*. The interferon score was determined based on the mean fold change of eight ISGs in each patient in comparison with the median of 10 healthy controls ⁴.

	Patient 1	Patient 2	Patient 3	Patient 4
<i>RAD51C</i> mutation	deletion exon 5-9	deletion exon 5-9	c.224_225insA p.Y75X	c.224_225insA p.Y75X
age	55 years	60 years	76 years	64 years
clinical findings	breast cancer, autoimmune thyroid disease	breast cancer, coronary heart disease	ovarian cancer, diabetes mellitus	ovarian cancer, autoimmune thyroid disease
serological findings	ANA 1:160 homogenous, fine granular [<1:80]		ANA 1:640 homogenous, fine granular [<1:80] C3d-CIC >200 µg/ml [<40]	
interferon score	195.1 [-0.35-0.37]	-29.6 [-0.35-0.37]	274.5 [-0.35-0.37]	-21.4 [-0.35-0.37]

Supplementary Table 2. Oligonucleotides used for quantitative real-time RT-PCR and microinjection. Oligonucleotides were purchased from Eurofins MWG Operon.

Name	Sequence (5' → 3')
IFNB_F	ACCTCCGAAACTGAAGATCTCCTA
IFNB_R	TGCTGGTTGAAGAATGCTTGA
IFNB_P	FAM-CCTGTGCCTCTGGGACTGGACAATTG-TAMRA
IFI27_F	AGCAGTGACCAGTGTGGCCAAAGT
IFI27_R	CTCCAATCACAACTGTAGCAATCC
IFI27_P	FAM-CCTCTGGCTCTGCCGTAGTTTTGCC-TAMRA
IFI44_F	TCTATTCAATACTTCTCCTCTCAGATGATAG
IFI44_R	TGAGCAAAGCCACATGTACCA
IFI44_P	FAM-CCAGCGTTTACCAACTCCCTTCGAATTCTT-TAMRA
GAPDH_F	GAAGGTGAAGGTCGGAGTC
GAPDH_R	GAAGATGGTGATGGGATTC
GAPDH_P	FAM-CAAGCTTCCCGTTCTCAGCC-TAMRA
ssDNA647N	ATTO647N-ATACGACGGTGACAGTGTGTCAGACAGGT
ssDNA488	ATTO488-CCTGTCTGACAACACTGTCACCGTCGTATG

Supplementary Notes

Clinical description of patients

Patient 1 (LE1) is a 51 year-old German female with systemic lupus erythematosus and a heterozygous TREX1 mutation (c.634delC; P212fs). She presented with plaques and papules on the back, neck and face since her early forties. Histology of lesional skin revealed perivascular lymphocytic infiltrates and sparse C3 deposits at the dermo-epidermal junction. She complained of photosensitivity, fatigue, recurrent fever and arthralgia of the knee, shoulder, spine and the mandibular joint. At 49 years of age she experienced a transient left sided hemiparesis, which resolved with minimal sequelae. Since that time she suffered from recurrent episodes of migraine. She also developed a depressive psychosis and increasing forgetfulness. Laboratory investigations were remarkable for intermittent lymphopenia (1.25 Gpt/l [1.5-4 Gpt/l]), and elevated γ -glutamate dehydrogenase (1.17 $\mu\text{mol}/(\text{s}^*l)$ [<0.7]). Antinuclear antibodies (ANA) were present with a maximum titre of 1:640 in a fine-speckled pattern. In addition, she was diagnosed with autoimmune thyroiditis and tested positive for anti-parietal cell antibodies. The patient responded well to hydroxychloroquine and intermittent prednisone in combination with sun protection. Her medical history also included surgical excision of a low grade melanoma on the back, a hysterectomy due to leukoplakia and treatment for invasive ductal carcinoma of the breast. Her family history was remarkable for her mother suffering from stroke and dementia, and her son suffering from photosensitive skin lesions and migraine since early adulthood.

Patient 2 (LE2) is a 45 year-old female from Germany with a familial chilblain lupus due to a heterozygous TREX1 mutation (c.52G>A; D18N). She suffered from cold-induced bluish-red inflammatory skin lesions on her fingers, toes, soles and shins since early childhood. In addition, she complained of arthralgia of knees and shoulders. On histological exam, lesional skin showed periadnexial and perivascular infiltrates. Her laboratory was remarkable for

antinuclear antibodies (1:160) and reduced complement C4 levels (0.15 g/l [0.164-0.392]). Her son and daughter were also affected.

Patient 3 (AGS1) is a 13 year-old boy of Turkish ancestry. His parents are first cousins. He was diagnosed with AGS due to a homozygous V201D (c.602T>A) TREX1 mutation. He was born at term with weight and head circumference within normal range. He presented with dystonia and hypotonia at three months of age. Magnetic resonance imaging (MRI) revealed extensive calcification of basal ganglia, myelin defects and atrophy. A lumbar puncture demonstrated lymphocytosis and raised IFN- α . He developed microcephaly, spastic tetraparesis and severe global developmental delay. He also suffered from chilblain lesions on the toes. He was diagnosed with type 1 diabetes mellitus at 7 years. At 10 years of age, he tested positive for ANA (1:160), anti-ENA (extractable nuclear antigens), cardiolipin-IgG 41.51 U/ml [<10] and anti-dsDNA 77.62 IU/ml [<30].

Patient 4 (AGS2) is a 19 year-old German male patient who carries the common R114H (c.341G>A) TREX1 mutation in the homozygous state. He was born at 36 weeks of gestation; his weight and head circumference were within normal limits for gestational age. He presented with hypotonia, seizures and dystonia at 4 months of age. He was found to have elevated IFN- α in cerebrospinal fluid. His MRI showed a leukencephalopathy with enlarged ventricles. He developed microcephaly and severe developmental delay. At the age of 17 years serologic testing revealed an ANA titre of 1:1280. He also tested positive for: anti-nucleosome 138.36 U/ml [<30], cardiolipin-IgG 15.5 U/ml [<10] and C3d circulating immune complexes 49.24 μ g/ml [<40].

Supplementary Methods

Immunolabeling for correlative light and electron microscopy. GFP-TREX1-transfected cells were fixed with 4% paraformaldehyde (PFA) in 0.1 M phosphate buffer (PB, pH 7.4) and processed for Tokuyasu cryo-sectioning using a Leica UC6 ultramicrotome equipped with a FC6 cryo-chamber. Dry-frozen ultrathin sections were picked up in methyl cellulose sucrose (1 part 2% methyl cellulose (Sigma) + 1 part 2.3 M sucrose) and transferred onto an electron microscopic support grid for subsequent immunogold labeling. Grids were placed upside down on drops of PBS, washed 5 times with 0.1% glycine/PBS, blocked with 1% BSA/PBS and incubated with anti-GFP-antibody (TP-401 from Torrey Pines; 1: 100) for 1 h. After washes in PBS, the sections were incubated with Protein A conjugated to 10 nm gold for 1 h, washed again in PBS and postfixed in 1% glutaraldehyde. Grids were washed several times in water, stained with neutral uranyl oxalate (2% UA in 0.15 M oxalic acid, pH7.0) for 5 min, washed shortly in water and incubated in methyl cellulose uranyl acetate (9 parts 2% MC + 1 part 4% UA, pH 4) on ice for 5 min. Finally, grids were looped out, the MC/UA film was reduced to an even thin film and air dried. The sections were analyzed on a Philips Morgagni 268 (FEI) at 80 kV and images were taken with the MegaView III digital camera (Olympus).

Western blot analysis, β -galactosidase staining, IFN reporter assay. Cells were lysed in RIPA buffer (50 mM Tris-HCl, pH 7.4, 150 mM NaCl, 1 mM EDTA, 1% Triton X-100, 1 mM sodium orthovanadate, 20 mM sodium fluoride) supplemented with 1x Complete Protease Inhibitor Cocktail and 1x PhosSTOP phosphatase inhibitors (Roche). Protein concentration was determined using a BCA Kit (Thermo Scientific). Lysates were subjected to SDS-PAGE and blotted onto a nitrocellulose membrane (BA83, Sigma-Aldrich). Membranes were blocked in 5% dry milk and probed using the following antibodies: anti-p53 (Ser15, sc-101762, Santa Cruz; 1:200), anti-p16 (sc-468, Santa Cruz; 1:1,000), anti-Chk1 (Ser345, 2348, Cell Signaling; 1:1,000), anti-pIRF3 (Ser386, ab76493, abcam, 1:500), anti-Rad51 (PC130, Merck; 1:500), anti-RPA (Cell Signaling, 1:1,000), anti-cGAS (Cell Signaling, 1:1,000) and anti- β -actin (clone AC-74, Sigma Aldrich; 1:10,000). Immunoreactive signals were detected by

chemiluminescence (Lumi-Light PLUS, Roche). Fibroblasts were stained using the Senescence β -Galactosidase Staining Kit (Cell Signaling) and analyzed by light microscopy. For quantification, cells of 8 randomly chosen fields were counted. IFN- β was measured by using HEK-Blue IFN- α/β cells (InvivoGen).

Cell cycle analysis by quantitative DNA imaging. Cell cycle analysis was performed by DNA content analysis based on the integrated DAPI intensity per nucleus ⁷. At least 100 fields of view were imaged per sample point using the Operetta high content imager (Perkin Elmer) equipped with a bandpass filter for DAPI (excitation: 360-400 nm; emission: 410-480 nm) using constant exposure times of 50 ms. Nuclear segmentation was performed by the Harmony software (Perkin Elmer) using method M and a guide size of 15 μ m diameter per nucleus. A split factor of 0.1 and local threshold were applied. Then the total nuclear DAPI intensity was measured. For fluorescent ubiquitination-based cell cycle indicator (Fucci) analysis ⁸, fibroblasts were transiently transfected with the two cell cycle reporter plasmids Fucci-G₁ Orange (monomeric Kusabira-Orange2-tagged Cdt1; Amalgaam Co.) and Fucci-S/G₂/M (monomeric Azami Green1-tagged geminin; Amalgaam Co.). While Fucci-G₁ Orange contains aa 30-120 of human Cdt1 and is only expressed in G₁, Fucci-S/G₂/M Green contains aa 1-60 of human Geminin and stains both nucleus and cytoplasm in green after G₁/S transition. Again the Operetta high content imager was used to record the images of DAPI as well as of monomeric Azami-Green1 (excitation: 460-490 nm; emission: 500-550 nm; exposure 300 ms) and monomeric Kusabira-Orange2 (excitation: 560-580 nm; emission: 590-640 nm; exposure 300 ms). Nuclear segmentation was done as described above and nuclear intensities in the red and green channel were measured accordingly. Cells expressing at least one of the two constructs were selected and plotted against the integrated DAPI intensity within the nucleus.

Immunohistochemistry. Fibroblasts grown on coverslips were fixed with 4% paraformaldehyde for 10 min and permeabilized for 5 min using 0.2% Triton X-100. To analyze

the detergent-extractable fraction of RPA, cells were first permeabilized for 5 min with 0.2% Triton X-100 followed by fixation with 4% paraformaldehyde for 10 min. After blocking with 1% BSA in PBS, slides were incubated with the following primary antibodies: anti-Rad51 (PC130, Merck; 1:500), anti-RPA (Cell Signaling, 1:1000). Slides were washed with 0.2% Tween in PBS and then incubated with the respective Alexa 488-conjugated secondary antibody (Invitrogen). Cells were mounted with VectaShield containing DAPI (Vector Labs). For high content automated imaging (Operetta, Perkin Elmer), a minimum of 100 fields of view were imaged per experimental sample using a 40x 0.95 NA air objective and analyzed with the Harmony software (Perkin Elmer). The following analysis sequence was applied: identify nuclei based on DAPI staining (method B), identify spots (method A) with relative spot intensity >0.04 and splitting coefficient =1. For each spot, contrast and mean intensity were calculated and spots with a intensity spot/spot area ratio >0.0015 selected to exclude nucleolar and weak background staining. In addition, the total nuclear intensity of RPA and Rad51 staining was measured. For staining of ssDNA, cells were first incubated with 0.1 mg/ml RNase A (Biozyme) in RNase A Buffer at 37°C for 30 min followed by incubation with or without 20 U/ml S1 nuclease in S1 nuclease-buffer (Applied Biosystems) at 37°C for 30 min. After blocking with 1% BSA in PBS, cells were stained with anti-ssDNA antibody (ABIN180204; 1:200). The signal was amplified by the secondary antibody using the Tyramide Signal Amplification Kit (Molecular Probes) and the mean fluorescence intensity from at least 65 cells per slide was determined using Image J. For subcellular analysis of TREX1, cells were treated with 6 mM hydroxyurea (Sigma) for 180 and 360 min, respectively, and then stained with anti-TREX1 (122115, Cell Signaling, 1:100) followed by the secondary antibody using the Tyramide Signal Amplification Kit (Molecular Probes). For staining of DNA double-strand breaks, fibroblasts or HeLa cells stably expressing mCherry-PCNA¹ were transfected with 200 ng of GFP-TREX1 or GFP-RNase H2B, respectively, and then probed with anti- γ H2AX (Ser139, clone 2F3, Novus Biologicals; 1:500) anti-53BP1 (NB100-904, Novus Biologicals; 1:2,000) followed by incubation with Alexa Fluor 546-conjugated goat-anti-mouse-IgG and Alexa Fluor 488-conjugated goat-anti-rabbit-IgG (Molecular Probes). Cells were mounted in VectaShield

Mounting Medium with DAPI (Vector Labs) and analyzed with a Zeiss Axioimager A1 microscope. For quantification, double stained foci in 50 randomly selected cells were counted per slide. For detection of CPDs, cells were fixed with methanol (-20°C) and acetone. DNA was denatured in 0.1 N NaOH. Cells were then dehydrated with increasing concentrations of ethanol (70-100%) and incubated with anti-CPD (clone KTM53, Kamiya Biomedical Company; 1:1,000) followed by staining with Alexa Fluor 488-conjugated goat-anti-mouse-IgG (Molecular Probes). The mean fluorescence intensity from 50 cells per slide was determined using Image J. For co-staining of RPA / Rad51 and ssDNA cells were imaged using a confocal laser scanning microscope (Leica SP5 II) equipped with HyD detectors operated in single photon counting mode. A confocal mid nuclear section was imaged using a CX PL APO 63x and images were quantified using Volocity (Perkin Elmer), a minimum of 10 cells were analyzed in two wild type cell lines and two AGS patient cell lines.

Raster image correlation spectroscopy. 2×10^4 cells per well were seeded in fibronectin-coated chambered glass slides (Nunc Lab-Tek), transfected with 10 ng of GFP-RPA32¹⁰ using FuGENE HD (Promega) and subjected to live cell imaging after 48 h. Raster image correlation spectroscopy (RICS)² was performed on an Zeiss confocal laser scanning microscope LSM 780 Axio Observer of the Light Microscopy Facility, a core facility of BIOTEC/CRTD at Technische Universität Dresden. Data were acquired and analyzed with the Zen 2.1 software (Zeiss). In detail, 64 x 64 pixel areas within the nucleus were analyzed (2-5 areas per nucleus) and spatial autocorrelation was calculated after detrending (immobile structures and stack) using the 3Dcoeff default formula for RICS. Each cell was visually inspected for focus drift and goodness of fit of the autocorrelation function. Time series were acquired with a pixel size of 51 nm and a pixel dwell time of 6.3 μ s using the 488 nm line of an Argon ion laser. A minimum of 10 cells was analyzed from each of two wild type and two AGS fibroblast cell lines.

Sytox Orange assay. HeLa-cells transfected with YFP-TREX1 were fixed in 4% paraformaldehyde and permeabilized with PBS containing 0.5% Triton-X 100 and 100 mM

glycine to block aldehyde groups. Digestion of nucleic acids was performed with 20 U/ml DNase I in DNase I-buffer (Applied Biosystems) at 37°C for 30 min. Cells were then stained with 5 μ M Sytox Orange (Molecular Probes) for 30 min, washed and mounted with VectaShield containing DAPI (Vector Labs). Fluorescence life time imaging analysis was carried out in the cytoplasm as previously described ¹¹ using a Zeiss Axiovert S100TV with a BL HC513/17 emission band-pass filter (Semrock). At least 20 cells were measured per experiment.

Microinjection, fluorescence cross-correlation spectroscopy. Cells were grown in MaTek chambers. Immediately before microinjection, the growth medium was replaced by air-buffer (150 mM NaCl, 20 mM HEPES pH 7.4, 15 mM Glucose, 150 μ g/ml BSA, 20 mM trehalose, 5.4 mM KCl, 0.85 mM MgSO₄, 0.6 mM CaCl₂). The micropipette (Femtotip 2, Eppendorf) was loaded with 2.5 μ l injection solution (110 mM K-gluconate, 18 mM NaCl, 10 mM Hepes pH 7.4, 0.6 mM MgSO₄) containing either 5 μ M ssDNA647N and 4 μ M 150 kDa FITC-dextran or 5 μ M dsDNA488_647N and 5 μ M 70 kDa Rhodamine B-dextran, respectively. Oligonucleotides were from IBA Life Sciences. Microinjection was carried out on an LSM780-Confocor3 microscope equipped with a microinjector consisting of a Femtojet and InjectMan NI2 (Eppendorf) mounted directly inside an incubation chamber at 37°C. Working pressure for injection was between 20-40 hPa for 0.1s and a holding pressure of 15 hPa. Fluorescence cross-correlation spectroscopy (FCCS) was used to assess exonuclease activity within the cytosol of living cells. FCCS is a highly sensitive biophysical technique for the study of the dynamics and interactions of two differently labeled molecule species in living cells. Two superimposed laser lines of different wavelength are focused by a single microscope objective in order to generate overlapping focal volume elements. In this way, two spectrally distinct dyes can be simultaneously excited and their fluorescence emission detected via the same objective in two separate channels. In fluid environments, diffusion of fluorescent molecules through the focal spot induces fluorescence fluctuation. Both fluctuating fluorescence signals are subjected to auto-correlation analysis. Additionally, the calculated cross-correlation function is obtained by correlating intensity fluctuations of both channels with each other. Only

when a dual-labeled molecule translocates through the detection volume it contributes to the cross-correlation curve. Hence, the amplitude of the cross-correlation curve is directly proportional to the amount of dual-labeled species and allows a quantitative analysis of interactions. Given that TREX1 also degrades dsDNA with 3' overhangs, we used a dual-labeled dsDNA oligonucleotide with 3' overhangs as substrate and measured exonucleolytic activity as loss of cross-correlation over time. FCCS was carried out directly after microinjection on the same microscope. Images were taken with low laser powers with spectral GaAsP-detector in photon counting mode. The 488 nm Ar-laser-line was used to excite ATTO488 and the 633 nm line was used to excite ATTO647N. Both laser lines were attenuated by an acousto-optical tunable filter to an intensity in the focal plane of 5.3 and 1.4 kW/cm², respectively, in order to minimize photobleaching and cellular damage. Both excitation laser lines were directed by a 488/633 dichroic mirror (MBS) onto the back aperture of a Zeiss C Apochromat 40x, N.A.=1.2, water immersion objective. The fluorescence light was collected by the same objective, separated from the excitation light by the MBS, passing a confocal pinhole (35 µm in diameter) and split into two spectral channels by a second dichroic (NFT, LP635). After removing residual laser light by a 505-610 nm bandpass and 655 nm longpass emission filter, respectively, the fluorescence light was recorded by avalanche photodiode detectors (APDs). The setup was adjusted using a dye mixture of Alexa488 and Alexa633. Before each experiment the amount of cross-correlation for the injected dsDNA (100 nM in injection buffer) was measured and used for normalization. The overall cross-correlation performance was determined with a 198 bp long ATTO488/ATTO647N double-labeled DNA yielding cross-correlation amplitudes of 75% (±5%). The discrepancy to 100% is due to imperfect overlap of the detection volumes and/or imperfect labeling of the DNA. FCCS was measured in the cytoplasm. At least 10 cells were measured per experiment in at least two independent experiments. Measurements were started as fast as possible after microinjection (approx. 15 min after injection start). For each measurement, 24 runs, each 10 sec long, were collected. The fluorescence signals of each run were software-correlated following the definition of auto- and cross-correlation as previously described ⁶.

Comet assay, halo assay. Alkaline single cell gel electrophoresis was performed as described ⁵. For halo assays ⁹, frosted microscope slides were pre-coated with melted 0.5% agarose (type II, Sigma) in PBS followed by 1% agarose (type II, Sigma). 1.5×10^4 cells synchronized by 24 h serum starvation were suspended in 150 μ l 3% low-melting point agarose (type VII, Sigma) melted in PBS at 50°C and dispersed on pre-warmed pre-coated slides. Fibroblasts were transfected with the indicated amount of a 45 bp oligonucleotide or plasmid DNA using polyethylenimine prior to synchronization. After gelling, slides were incubated in alkaline lysis buffer (2.5 M NaCl, 0.1 M EDTA, 10 mM Tris, 1% Triton X-100, pH 10) at 4°C for 18 h. Slides were then washed 10 times for 10 min in PBS. After neutralization in 0.5M Tris-HCl for 30 min, 200 μ l Antifade with Sybr Gold (20 mM DABCO, 0.1 μ l/ml Sybr Gold, 20 mM Tris-HCl, 80% glycerol) was added to each slide and covered with a cover slip. Microscopy was carried out at 10x magnification. Images were captured using constant exposure times and a minimum of 50 cells per slide was analyzed using Image J. Single nuclei were cropped and adjacent background was subtracted. A vertical and horizontal intensity profile was measured. Based on the intensity profile the distance between the 10% maximum intensities of the left and right flanks (upper and lower, respectively) was calculated for each nucleus. For cumulative curves the intensity profiles were centered to the maximum position and normalized to the maximum intensity value. Then mean profiles were calculated for each population.

RNA sequencing. RNA sequencing was performed as previously described ⁵. RNA sequencing data were submitted to the Gene Expression Omnibus (GEO) under accession number GSE59233. Transcriptome analysis of shRNA-induced knockout of RPA in MEFs (GSE38412) and of Rad51 in MCF-10A mammary epithelial cells (GSE54266), respectively, was carried out using published datasets retrieved from the GEO database (www.ncbi.nlm.nih.gov/geo). Differential gene expression was analyzed using GEO2R by comparing gene expression profiles of each group (n = 3 for RPA; n = 4 for Rad51) with those

of the respective control groups treated with scrambled shRNA (n = 3 per group). Fold changes in ISGs expression with an adjusted $P < 0.05$ were considered significant.

Supplementary References

1. Chagin, V. O., Casas-Delucchi, C. S., Reinhart, M., Schermelleh, L., Markaki, Y., Maiser, A., Bolius, J.J., Bensimon, A., Fillies, M., Domaing, P., Rozanov, Y.M., Leonhardt, H. & Cardoso, M.C. 4D Visualization of replication foci in mammalian cells corresponding to individual replicons. *Nat. Commun.* **7**, doi:10.1038/ncomms11231 (2016).
2. Digman, M. A., Brown, C. M., Sengupta, P., Wiseman, P. W., Horwitz, A. R. & Gratton, E. Measuring fast dynamics in solutions and cells with a laser scanning microscope. *Biophys. J.* **89**, 1317-1327 (2005).
3. Dross, N., Spriet, C., Zwerger, M., Muller, G., Waldeck, W. & Langowski, J. Mapping eGFP oligomer mobility in living cell nuclei. *PLoS. One.* **4**, e5041 (2009).
4. Feng, X., Wu, H., Grossman, J. M., Hanvivadhanakul, P., FitzGerald, J. D., Park, G. S. *et al.* Association of increased interferon-inducible gene expression with disease activity and lupus nephritis in patients with systemic lupus erythematosus. *Arthritis Rheum.* **54**, 2951-2962 (2006).
5. Kretschmer, S., Wolf, C., Konig, N., Staroske, W., Guck, J., Hausler, M. *et al.* SAMHD1 prevents autoimmunity by maintaining genome stability. *Ann. Rheum. Dis.* **74**, e17 (2015).
6. Ohrt, T., Staroske, W., Mutze, J., Crell, K., Landthaler, M. & Schwille, P. Fluorescence cross-correlation spectroscopy reveals mechanistic insights into the effect of 2'-O-methyl modified siRNAs in living cells. *Biophys. J.* **100**, 2981-2990 (2011).
7. Roukos, V., Pegoraro, G., Voss, T. C. & Misteli, T. Cell cycle staging of individual cells by fluorescence microscopy. *Nat. Protoc.* **10**, 334-348 (2015).
8. Sakaue-Sawano, A., Kurokawa, H., Morimura, T., Hanyu, A., Hama, H., Osawa, H. *et al.* Visualizing spatiotemporal dynamics of multicellular cell-cycle progression. *Cell* **132**, 487-498 (2008).
9. Sestili, P. The fast-halo assay for the assessment of DNA damage at the single-cell level. *Methods Mol. Biol.* **521**, 517-533 (2009).

10. Sporbert, A., Gahl, A., Ankerhold, R., Leonhardt, H. & Cardoso, M. C. DNA polymerase clamp shows little turnover at established replication sites but sequential de novo assembly at adjacent origin clusters. *Mol. Cell* **10**, 1355-1365 (2002).
11. Tungler, V., Staroske, W., Kind, B., Dobrick, M., Kretschmer, S., Schmidt, F. *et al.* Single-stranded nucleic acids promote SAMHD1 complex formation. *J. Mol. Med. (Berl)* **91**, 759-770 (2013).